Understanding and Managing Identification Uncertainty

of Close Modes in Operational Modal Analysis

Siu-Kui Au [1], James M.W. Brownjohn [2], Binbin Li [3], Alison Raby [4]

Abstract

Close modes are much more difficult to identify than well-separated modes and their identification (ID) results often have significantly larger uncertainty or variability. The situation becomes even more challenging in operational modal analysis (OMA), which is currently the most economically viable means for obtaining in-situ dynamic properties of large civil structures and where ID uncertainty management is most needed. To understand ID uncertainty and manage it in field test planning, this work develops the 'uncertainty law' for close modes, i.e., closed form analytical expressions for the remaining uncertainty of modal parameters identified using output-only ambient vibration data. The expressions reveal a fundamental definition that quantifies 'how close is close' and demystify the roles of various governing factors. The results are verified with synthetic, laboratory and field data. Statistics of governing factors from field data reveal OMA challenges in different situations, now accountable within a coherent probabilistic framework. Recommendations are made for planning ambient vibration tests taking close modes into account. Up to modelling assumptions and the use of probability, the uncertainty law dictates the achievable precision of modal properties regardless of the ID algorithm used. The mathematical theory behind the results in this paper is presented in a companion paper.

Keywords: ambient modal identification, BAYOMA, close modes, Fisher Information Matrix, operational modal analysis, uncertainty law

---

[1] School of Civil and Environmental Engineering, Nanyang Technological University, 50 Nanyang Avenue, Singapore 639798. E-mail: ivanau@ntu.edu.sg

[2] Director, Full Scale Dynamics Limited, The Innovation Centre, 217 Portobello, Sheffield S1 4DP, UK; College of Engineering Mathematics and Physical Sciences (CEMPS), University of Exeter, Harrison Building, Exeter EX4 4QF, UK. E-mail: J.Brownjohn@Exeter.ac.uk

[3] Corresponding author. ZJU-UIUC Institute, Zhejiang University, Haining, 314400, China. Email: bbl@zju.edu.cn

[4] School of Engineering, Computing and Mathematics, University of Plymouth, Drake Circus, Plymouth, PL4 8AA, UK. Email: alison.raby@plymouth.ac.uk

1 Introduction

The modal properties of a structure include primarily the natural frequencies, mode shapes and damping ratios. They are the interface between the physical properties (e.g., stiffness and mass) and response of a structure. Modal identification (ID) aims at back-calculating the modal properties from vibration data. It provides vital information for understanding the as-built characteristics of a structure without tracing back to physical properties whose identification is less well-defined and can be much more challenging depending on the complexity of structural model used. Modal ID is demanded for many downstream applications, e.g., vibration diagnosis, control, model updating [1] and structural health monitoring [2][3][4]. A comprehensive report on structural system identification of constructed facilities can be found in [5].

The nature of input loading and whether it can be controlled or known (measured) during the test govern the choice of ID algorithm and the achievable ID precision. A traditional means is 'experimental modal analysis' (EMA) [6][7] where the input is controlled to achieve a good signal-to-noise (s/n) ratio for modal ID. Generating or controlling the input to dominate response is expensive and typically impossible for large structures where the ambient response from fixtures and environment is already difficult to beat. Operational modal analysis (OMA) [8][9][10] aims at modal ID using 'output-only' vibration data without knowing the input excitations. It significantly improves feasibility and implementation economy, showing great promise for regular practice in the near future. In OMA, the unknown input is typically modelled by a stochastic process with constant spectral properties, e.g., white or band-limited white within the resonance bands of interest. This allows the spectral characteristics of the measured response to be governed by modal properties of interest, making them identifiable and distinguishable from the loading. For a similar reason, vibration modes are intuitively more distinguishable (hence identified) when their frequencies are 'well-separated' than 'closely-spaced'.

There is currently no formal quantitative definition for close modes, but qualitatively their frequencies are so close that their resonance bands overlap, e.g., visually in the power spectral density (PSD) or singular value (SV) spectrum of data [11]. Compared to well-separated modes, close modes are not as common but they do occur and carry significance. They most typically occur in various forms of tower with two or more horizontal axes of symmetry, e.g., tall buildings [12][13], telecommunication (guyed) masts and freestanding lattice towers [14], cylindrical chimneys [15][16], space launchers [17] and lighthouses [18]. For tall buildings the stiffness and mass properties along two horizontal principal directions can be very similar by design. For the other structures symmetry and resultant close modes are a natural consequence of the structural form adopted to fulfil their

function against environmental (usually wind) loads. Identifying close modes is important for these structures because they are the effect of subtle differences in stiffness and mass distribution within the almost symmetric structure. For cylindrical industrial chimneys the differences are due to openings at the base, e.g., for flue gas, whereas for lighthouses they are the consequence of masonry coursework adapting to the foundation rock topology. Close modes can be found by chance in other structures, e.g., Humber Bridge [19] where closeness of torsional and vertical mode frequencies can affect in-wind dynamics by aeroelasticity.

Predicting response comprising close modes under ambient excitations (as in OMA) is more difficult compared to well-separated modes because of the correlation arising from modal forces. Early analytical work on the correlation of response [20] led to the 'complete quadratic combination' (CQC) rule in earthquake engineering [21][22]. Theoretically, the full mode shapes comprising all degrees of freedom (DOFs) satisfying the generalised eigenvalue problem are arbitrary for repeated, i.e., identical, natural frequencies. In reality, natural frequencies are rarely identical (at least difficult to prove experimentally) because of imperfections; and mode shapes with close frequencies are found to be sensitive to physical conditions. A higher order MAC (modal assurance criterion) of mode shapes has been defined for close modes in terms of the subspace containing them [23]. A perturbation study [24][25] shows that the increased sensitivity is characterised by rotations within the 'mode shape subspace' (MSS) spanned by the mode shapes. Such rotations are inversely proportional to the fractional difference of frequencies.

It comes with no surprise that close modes are much more difficult to identify than well-separated modes. Since their frequencies are close, their detection requires as many measured DOFs (as the number of modes) along directions spanning the MSS so that the data PSD matrix has sufficient rank to show multiple significant lines in the SV spectrum. This is not required for well-separated modes because they can be detected by distinct peaks in the SV spectrum, for example. In some special cases where the close modes dominate different groups of measured DOFs, post-processing tricks can be used to separate them so that a single mode algorithm can be used, e.g., taking sum and difference of vertical response on either side of a suspension bridge deck to separate close vertical and torsional modes; or applying a rotational transformation to the bi-directional signals from a quasi-axisymmetric structure to separate the modes.

Catering for close modes in the ID method requires much sophistication in mathematics and computation especially for frequency domain methods. The 'entangling' of modal properties in the frequency response functions (FRF) and mode shapes (which need not be orthogonal because of limited measured DOFs) makes it difficult to separate spectral (e.g., frequency and damping) and

spatial (mode shape) properties by matrix-decomposition of the PSD matrix (or variant), except for uncorrelated modal forces and orthogonal measured mode shapes. Reference [26] discussed a potential over-estimation of damping ratio in FDD (Frequency Domain Decomposition) due to leakage in the estimated PSD. An enhanced PSD through modal filtering was proposed in [27] to improve the estimation of frequencies and damping ratios of close modes, although issues still remain for mode shapes. Bayesian Operational Modal Analysis (BAYOMA) methodology operating in the frequency domain and applicable for close modes has been developed [28]; see [10] for a monograph. The linear algebra and programming effort is much more involved than the well-separated mode counterpart [29]. See also [30] for a recent development based on expectation-maximisation algorithm that shows promise for simpler algorithm and computer-coding. Time domain algorithms are less directly affected by the presence of close modes. Examples with close modes can be found in [31][32] for NeXT-ERA (Natural Excitation Eigen-Realisation Technique) and [33][34][35] for SSI (Stochastic Subspace Identification).
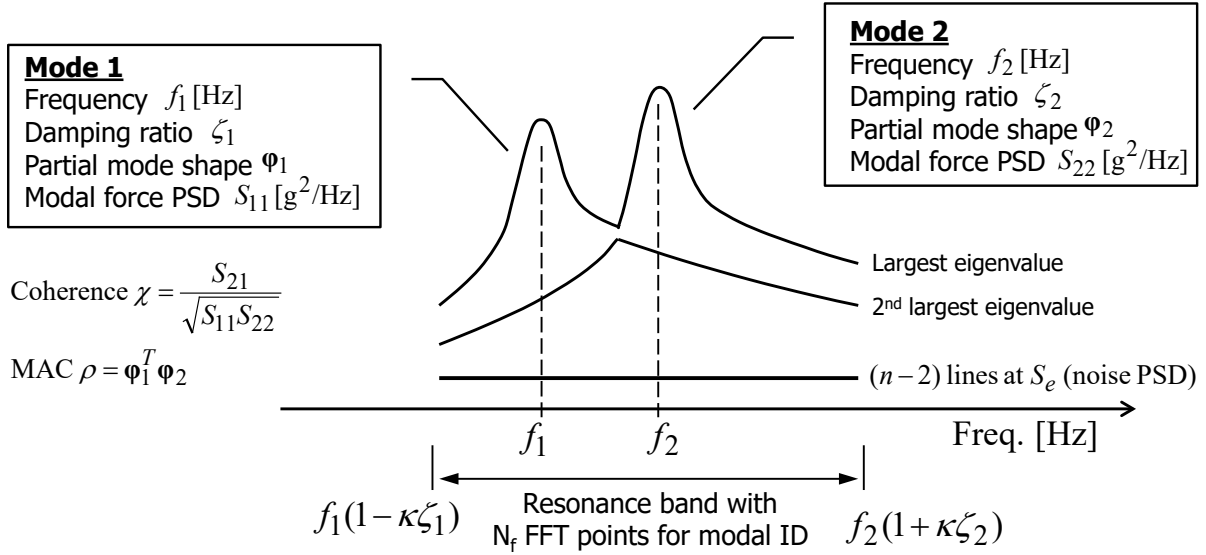
Regardless of ID method, it is commonly perceived that the identification error or uncertainty associated with close modes is significantly higher than well-separated modes, although there is no full account on the actual mechanism or quantification. An empirical study in [36] reveals that the quality of ID results generally deteriorates when the modes are 'close' in the sense that the fractional difference of frequencies normalised by damping ratio is small. This is also evident in a parametric study based on synthetic data identified by BAYOMA [37]. See also [38] and other references mentioned herein.

As part of a research campaign to understand and manage ID uncertainty in OMA, this work develops closed form expressions, referred as 'uncertainty law', that explicitly relate the ID uncertainty of close modes in OMA to test configuration. This contributes to a significant advancement beyond previous work for well-separated modes [39]. For the complexity of the theory involved and to facilitate reading and appreciation of significance, this work is presented in two companion papers. This paper presents the key results and implications, followed by verifications with synthetic, laboratory and field data; and finally recommendations for planning field vibration tests. The mathematical theory is presented in the companion paper [40]. A Bayesian modal ID approach based on the Fast Fourier Transform (FFT) on the resonance band of close modes, i.e., the same context of BAYOMA, is assumed in the derivation. Up to the same (conventional) modelling assumptions, the expressions for ID uncertainty dictate the achievable precision of any other methods because there is a 1-1 correspondence between the time domain data and its FFT (so no

loss of information); and probabilistic information in data has been processed in a consistent manner following rigorously Bayes' rules.

2 Wideband uncertainty law (key theoretical results)

We first summarise the assumptions and key theoretical findings on ID uncertainty of close modes. They are proven in the companion paper and will be discussed qualitatively in Section 3. Consider two classically damped modes ($i = 1, 2$) with natural frequencies f_i (Hz), damping ratios ζ_i and mode shapes $\boldsymbol{\varphi}_i$ (real-valued, confined to measured DOFs and normalised with unit sum of squares), subjected to ambient excitations whose modal forces are assumed to be stochastic stationary with constant PSDs S_{ii} (g^2 / Hz) and coherence $\chi = S_{21} / \sqrt{S_{11} S_{22}}$ (complex-valued) within the resonance band covering the two modes (so only band-limited white). Specifically, for the familiar structural dynamics equation $\mathbf{M\ddot{x}} + \mathbf{C\dot{x}} + \mathbf{Kx} = \mathbf{F}$, the modal force here is per unit modal mass and defined as $p_i = (\boldsymbol{\psi}_i^T \mathbf{F}) / (\boldsymbol{\psi}_i^T \mathbf{M} \boldsymbol{\psi}_i)$, where $\boldsymbol{\psi}_i$ is the full mode shape comprising all (possibly infinitely many) DOFs. Without loss of generality, acceleration data is used for identifying the modes. It is contaminated by independent and identically distributed (i.i.d.) noise among different measured DOFs with a PSD of S_e (g^2 / Hz) within the resonance band (so only band-limited white). The resonance band is represented by $[f_1(1 - \kappa\zeta_1), f_2(1 + \kappa\zeta_2)]$ (Hz), which has N_f FFT points as 'data' in the Bayes' theorem for modal identification; κ is a dimensionless 'bandwidth factor'. This is illustrated in Figure 1. We assume that $|\chi| < 1$ (imperfect modal force coherence) and $|\rho| < 1$ (linearly independent mode shapes; $\rho =$ modal assurance criterion), for otherwise the problem degenerates and requires a separate formal analysis. Effectively, this work assumes that the subject close modes can be 'detected', e.g., from observation of multiple lines displaying dynamic amplification, as illustrated in Figure 1. The general question of detecting (close) modes is related to, e.g., whether the modes are well excited beyond noise level and whether the measured DOFs allow the mode shapes to be distinguished. While the question of detecting modes is important and is often addressed empirically, its theoretical treatment is out of the present scope.

Mode 1
Frequency f_1 [Hz]
Damping ratio ζ_1
Partial mode shape φ_1
Modal force PSD S_{11} [g^2/Hz]

Mode 2
Frequency f_2 [Hz]
Damping ratio ζ_2
Partial mode shape φ_2
Modal force PSD S_{22} [g^2/Hz]

Coherence $\chi = \dfrac{S_{21}}{\sqrt{S_{11}S_{22}}}$

MAC $\rho = \varphi_1^T \varphi_2$

Largest eigenvalue

2nd largest eigenvalue

$(n-2)$ lines at S_e (noise PSD)

Freq. [Hz]

f_1 f_2

$f_1(1-\kappa\zeta_1)$ Resonance band with N_f FFT points for modal ID $f_2(1+\kappa\zeta_2)$

Figure 1 Schematic diagram showing the theoretical singular value spectrum of ambient data on a resonance band with two close modes

In the above context, we have obtained analytical expressions for the 'remaining', i.e., ID uncertainty, of the natural frequencies, damping ratios and mode shapes identified based on information from data through its FFT in the resonance band. The results are collectively referred as 'uncertainty law' (for close modes). ID uncertainty is quantified in terms of a coefficient of variation (c.o.v. = standard deviation/mean). The expressions relate the ID uncertainty to the 'true' modal properties that are assumed to have given rise to the data. They are 'asymptotic expressions' in the sense that they have been derived for long data ($N_f \gg 1$), high signal-to-noise (s/n) ratio, small damping and wide resonance band ($\kappa \gg 1$ and $\kappa \gg e_i$; see later). These assumptions, except for wide resonance band, were adopted in previous studies of well-separated modes [39]. Empirically, one may think of, e.g., $N_f > 30$, $\kappa > 5$ and s/n ratio >100 meeting these requirements. Wide band is the condition under which we are currently able to obtain mathematically rigorous and insightful expressions for ID uncertainty of close modes. A mathematically rigorous theory that accounts for the effect of finite bandwidth and s/n ratio has not been developed but these are addressed by empirical factors; see Table 1 in Section 4. Although this work assumes acceleration data in its development, it is also applicable to other data types (e.g., velocity, displacement) provided that the s/n ratio is defined in a consistent manner with the data type; see Section 6.6 in the companion paper.

In reality, the noise PSDs of different channels are never the same but the uncertainty law is robust to this modelling error unless the PSDs differ by orders of magnitude. This is because the uncertainty of the noise PSDs is asymptotically uncorrelated from the remaining parameters. When applying the

6

uncertainty law for cases with a large channel noise disparity, one may use a value of S_e with a representative order of magnitude, e.g., the geometric mean. The effect of 'leakage', i.e., smearing of energy over neighbouring frequencies in FFT, is neglected in the scope of uncertainty law because it is asymptotically small for long data.

2.1 Mode shape

Mode shape uncertainty is most intriguing, revealing all governing factors and so it is presented first. As a background, it was found in a recent study [41] that for close modes there are two types of ID uncertainties: one (Type 1) orthogonal to the mode shape subspace (MSS) spanned by the mode shapes, and the other (Type 2) within the MSS. Type 1 was found in well-separated modes but Type 2 is unique to close modes. See Figure 2 for an illustration with $n = 3$ measured DOFs. It was shown that Type 1 and Type 2 uncertainties are asymptotically uncorrelated (a nice result but not trivial) and so the total variance is simply the sum of their individual variances. Mode shape is a vector-valued quantity subjected to norm constraint. Its uncertainty can be measured by the 'mode shape c.o.v.', defined as the square root sum of eigenvalues of the mode shape covariance matrix (see Section 11.3 of [10]). For small uncertainty it can be interpreted as the mean value of the hyper-angle the uncertain mode shape makes with its mean position. Figure 3 illustrates visually the uncertainty associated with different levels of mode shape c.o.v.. The demarcations are suggested as rule of thumb but otherwise subjective.
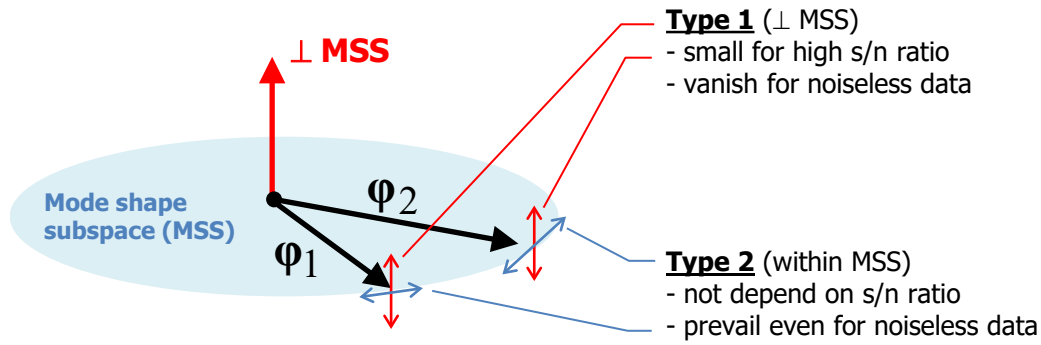
Figure 2 Illustration of mode shape uncertainty for two modes identified with data of high s/n ratio and $n = 3$ measured DOFs. Type 1 and Type 2 uncertainties are uncorrelated. See (2) and (3) for their c.o.v.s for wide band and Table 1 for empirical factors to account for bandwidth and s/n ratio
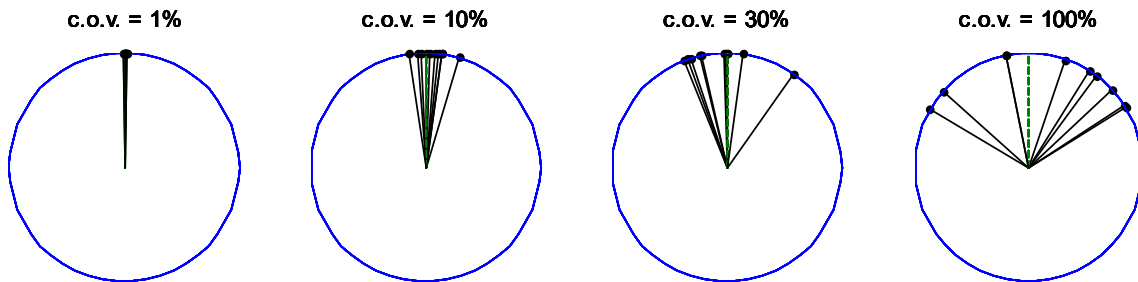

Figure 3 Illustration of mode shape uncertainty at different c.o.v. levels. Each plot shows ten randomly generated mode shapes with a mean pointing North and a mode shape c.o.v. of 1% (accurate), 10% (acceptable), 30% (border line), 100% (almost unidentifiable)

For a given mode i, the square of mode shape c.o.v., $\delta_{\varphi i}^2$, comprises contributions from the two types:

$$\delta_{\varphi i}^2 \sim \delta_{\varphi i}'^2 + \delta_{\varphi i}''^2 \qquad (1)$$

where $\delta_{\varphi i}'$ and $\delta_{\varphi i}''$ are the c.o.v.s of Type 1 and Type 2, respectively; '~' is to be read mathematically as 'asymptotic to', i.e., the ratio of the two sides tends to 1 under the stated asymptotic conditions, i.e., long data, high s/n ratio, etc. In this work we show (see Section 9 of companion paper) that Type 1 mode shape c.o.v. is given by a product of factors:

$$\delta_{\varphi i}'^2 = \underbrace{\frac{1}{2\pi\zeta_i N_{ci}} \times \overbrace{\frac{1}{\gamma_i'}}^{\text{s/n effect}} \times \overbrace{(n-2)}^{\substack{\text{Dim.} \perp \\ \text{to MSS}}} }_{\substack{\text{analogous to well-} \\ \text{separated modes}}} \times \underbrace{\frac{1}{1-q_2^2\,|\chi|^2}}_{\substack{\text{coherence} \\ \text{effect}}} \qquad\qquad \gamma_i' = \frac{S_{ii}}{4S_e\zeta_i^2} \qquad\qquad (2)$$

where the influences due to the different factors have been indicated and will be discussed later in Section 3; γ_i' is the modal s/n ratio defined previously for well-separated modes [39]; $N_{ci} = T_d f_i$ is a dimensionless data duration as a multiple of natural period; q_2 will be described shortly. On the other hand, Type 2 mode shape c.o.v. is given by a product of factors, all except one different from Type 1 (see Section 6.4 of companion paper for proof):

$$\delta_{\varphi i}''^2 \sim \frac{1}{2\pi\zeta_i N_{ci}} \times \underbrace{(1-\rho^2)}_{\substack{\text{MAC} \\ \text{effect}}} \times \underbrace{\frac{S_{jj}}{S_{ii}}}_{\substack{\text{disparity} \\ \text{in modal} \\ \text{force PSD}}} \times \underbrace{\frac{1}{d_i^2}}_{\substack{\text{disparity} \\ \text{in freq. and} \\ \text{damping}}} \times \underbrace{Q_{\varphi i}}_{\substack{\text{coherence} \\ \text{effect}}} \qquad\qquad (3)$$

where j refers to the index of the other mode, i.e., $j=2$ for $i=1$ and $j=1$ for $i=2$;

$$Q_{\varphi i} = \frac{1-q_2^2\,|\chi|^4}{(1-q_1^2\,|\chi|^4)(1-q_2^2\,|\chi|^2)} \qquad\qquad (4)$$

is a 'coherence factor' carrying the amplification due to modal force coherence;

$$q_1 = q_2\sin(2\phi - \psi) \qquad\qquad q_2 = \sqrt{g_1^2 + g_2^2} \qquad\qquad (\,\tan\psi = \frac{g_1}{g_2}\,,\ \phi = \angle\chi\,) \qquad (5)$$

$$g_1 = \frac{2\sqrt{(2+c_1)(2+c_2)}}{|e_1 e_2| + (2+c_1)(2+c_2)} \qquad\qquad g_2 = \frac{2\sqrt{|e_1 e_2|}}{|e_1 e_2| + (2+c_1)(2+c_2)} \qquad\qquad (6)$$

are 'modal entangling factors' induced by the following 'disparity' parameters that quantify how the two modes differ (in addition to modal force) in damping, frequency and in an overall sense, respectively:

$$c_i = \frac{f_j\zeta_j}{f_i\zeta_i} - 1 \qquad\qquad e_i = \frac{f_j - f_i}{f_i\zeta_i} \qquad\qquad d_i = \sqrt{c_i^2 + e_i^2} \qquad\qquad (7)$$

The modal entangling factors in (5) and (6) are not intuitive but they carry the mechanism by which frequency and damping disparities mix together with modal force coherence to affect ID uncertainty.

9

See Figure 6 later for a geometric interpretation. The definitions of the above parameters are motivated from the analytical expressions of the c.o.v.s, i.e., they carry fundamental significance instead of being empirically defined. See Table 7 of the companion paper for a summary.

2.2 Natural frequencies and damping ratios

Compared to mode shapes, the ID uncertainty of frequencies and damping ratios for close modes are affected in a less systematic manner by disparity. They are only correlated with Type 2 mode shape uncertainty. We show that the c.o.v. of natural frequencies δ_{f_i} and damping ratios δ_{ζ_i} are given by (see Section 6.5 of companion paper for proof)

$$
\delta_{f_i}^2 \sim \underbrace{\frac{\zeta_i}{2\pi N_{ci}}}_{\substack{\text{same for well-} \\ \text{separated modes}}} \times \underbrace{Q_{f_i}}_{\substack{\text{coherence} \\ \text{effect}}}
\tag{8}
$$

$$
\delta_{\zeta_i}^2 \sim \underbrace{\frac{1}{2\pi \zeta_i N_{ci}}}_{\substack{\text{same for well-} \\ \text{separated modes}}} \times \underbrace{Q_{\zeta_i}}_{\substack{\text{coherence} \\ \text{effect}}}
\tag{9}
$$

where Q_{f_i} and Q_{ζ_i} are coherence factors given by:

$$
Q_{f_i} = \frac{1-|\chi|^2}{1-q_2^2\,|\chi|^4} + \frac{|\chi|^2\,R_{f_i}}{(1-q_2^2\,|\chi|^2)(1-q_1^2\,|\chi|^4)(1-q_2^2\,|\chi|^4)}
\tag{10}
$$

$$
Q_{\zeta_i} = \frac{1-|\chi|^2}{1-q_2^2\,|\chi|^4} + \frac{|\chi|^2\,R_{\zeta_i}}{(1-q_2^2\,|\chi|^2)(1-q_1^2\,|\chi|^4)(1-q_2^2\,|\chi|^4)}
\tag{11}
$$

R_{f_i} and R_{ζ_i} are factors that depend on the phase angles ϕ, ψ and $\phi_i = \tan^{-1} c_i / e_i$:

$$
\begin{aligned}
R_{f_i} = {} & (1-q_2^2\,|\chi|^2)^2 \cos^2(\phi - s_i\phi_i) + (1-|\chi|^2)^2 q_2^2 \sin^2(\phi + s_i\phi_i - \psi) \\
& + 2q_1 q_2\,|\chi|^2\,(1-q_2^2\,|\chi|^2)(1-|\chi|^2)\cos(\phi - s_i\phi_i)\sin(\phi + s_i\phi_i - \psi)
\end{aligned}
\tag{12}
$$

$$
\begin{aligned}
R_{\zeta_i} = {} & (1-q_2^2\,|\chi|^2)^2 \sin^2(\phi - s_i\phi_i) + (1-|\chi|^2)^2 q_2^2 \cos^2(\phi + s_i\phi_i - \psi) \\
& + 2q_1 q_2\,|\chi|^2\,(1-q_2^2\,|\chi|^2)(1-|\chi|^2)\sin(\phi - s_i\phi_i)\cos(\phi + s_i\phi_i - \psi)
\end{aligned}
\tag{13}
$$

where $s_1 = 1$ and $s_2 = -1$. Note that swapping the sines and cosines in R_{f_i} gives R_{ζ_i}.

3 Qualitative analysis and insights

As uncertainty law, (1), (8) and (9) give the leading order value of the remaining uncertainty about the modal properties identified from ambient vibration data under test configuration and environment quantified by various parameters in the formulae. The uncertainty law involves a combination of Bayesian and frequentist concept. The value calculated from the formula is not exactly the value of 'posterior' (i.e., given data) uncertainty in a Bayesian context; it cannot be, since such value should depend on data. However, assuming that the data indeed obeys modelling assumptions and results from some 'true' parameter values (as appearing in the formulae; a frequentist assumption) then for long data, high s/n ratio and wide band their ratio will tend to 1. Similar to the Laws of Large Numbers in statistics, this is only a theoretical statement because in reality data never obeys modelling assumptions perfectly and 'true' parameter values need not exist in the real world. In a Bayesian perspective, the belief of true parameter values is referred as 'mind-projection fallacy' [42][43]. However, it is this type of statement that serves the purpose of understanding and managing uncertainty before data is available.

3.1 Uncertainty law and Fisher Information Matrix

How is the uncertainty law derived? In the context just mentioned, for long data the posterior covariance matrix (Bayesian) of modal parameters is equal to the inverse of the 'Fisher Information Matrix' (FIM, frequentist). The FIM is a real-symmetric matrix with dimension equal to the number of parameters to be identified in the problem. For the present OMA problem where the FFTs of data are asymptotically independent with a joint complex Gaussian distribution, standard results (e.g., Section 9.4 of [10]) show that the entry in the FIM corresponding to modal parameters x and y is equal to

$$J_{xy} = tr\Sigma[\mathbf{E}_k^{-1}\mathbf{E}_k^{(x)}\mathbf{E}_k^{-1}\mathbf{E}_k^{(y)}] \tag{14}$$

where $tr(\cdot)$ denotes the 'trace' (i.e., sum of diagonal entries) of the argument matrix; $\mathbf{E}_k$ is the theoretical data PSD matrix (evaluated at true parameter values) at FFT frequency $\mathbf{f}_k$ and the sum is over all frequencies in the selected band; see equation (1) for details in the companion paper [40]. This 'exact' FIM is applicable for general situations, i.e., even under non-asymptotic situations of low s/n ratio, limited band, etc. However, it does not offer any insights to serve the purpose of uncertainty law. The formulae in (1), (8) and (9) involve a tremendous effort to obtain the *diagonal entries of the inverse of FIM in analytical form*, though under asymptotic conditions that have been discovered to allow this possibility which should not be taken for granted. See the companion paper for derivation details.

3.2 What difference do close modes make?

For instructional purpose it is useful to review the uncertainty law for well-separated modes so that we can see what difference the close mode problem makes and what factors matter. For well-separated modes identified with a wide resonance band, the c.o.v.s are given by [39]

$$\delta^2_{\boldsymbol{\varphi}i} \sim \frac{1}{2\pi\zeta_i N_{ci}} \times \frac{1}{\gamma'_i} \times (n-1) \qquad\qquad \delta^2_{f_i} \sim \frac{\zeta_i}{2\pi N_{ci}} \qquad\qquad \delta^2_{\zeta_i} \sim \frac{1}{2\pi\zeta_i N_{ci}} \tag{15}$$

The c.o.v.s in (2), (3), (8) and (9) have been written as the values for well-separated modes multiplied by various effects brought by close modes. The c.o.v.s of frequencies and damping ratios are only affected by modal force coherence χ through Q_{f_i} and Q_{ζ_i}. Mode shapes are affected by all factors in the problem, i.e., modal force coherence through $Q_{\boldsymbol{\varphi}i}$, difference in frequencies and damping ratios through d_i, difference in modal force PSD through S_{jj}/S_{ii} and difference in mode shapes through the MAC ρ.

So what difference does it make when two modes are close rather than well-separated? For frequencies and damping ratios, (8) and (9) say that if $\chi = 0$ (perfectly incoherent modal forces) then it makes no difference, since then Q_{f_i} and Q_{ζ_i} are both equal to unity. For mode shapes, as long as the two modes are identified (and hence modelled) together on the same band they tend to have a higher uncertainty than if they were not, due to the new dimension of uncertainty within the MSS. As an example, consider two close modes with zero modal force coherence ($\chi = 0$) and orthogonal mode shapes at the measured DOFs ($\rho = 0$). This is a case where the modes are perceived to be clearly distinguishable; and where the 'operational deflection shapes' obtained by matrix decomposition of the data PSD matrix coincide with the physical mode shapes $\boldsymbol{\varphi}_i$. According to (1),

$$\delta^2_{\boldsymbol{\varphi}i} \sim \underbrace{\frac{n-2}{2\pi\zeta_i N_{ci}\gamma_i}}_{\text{Type 1},\,\perp\text{MSS}} + \underbrace{\frac{1}{2\pi\zeta_i N_{ci}} \times \frac{S_{jj}}{S_{ii}} \times \frac{1}{d_i^2}}_{\text{Type 2, within MSS}} \qquad\qquad (\chi = 0, \rho = 0) \tag{16}$$

which still depends on the disparities in frequencies, damping ratios and modal force PSDs. Essentially, once we allow the mode shapes to 'trade' within their MSS to 'fit' the data, there is always a component of uncertainty within the MSS that will not vanish even for noiseless data. Such uncertainty is amplified when the subject mode has a lower PSD than the other mode ($S_{jj}/S_{ii} > 1$),

or when the two modes get closer (smaller d_i). In Sections 3.3 to 3.5 to follow, we discuss systematically the effect of modal disparity (i.e., how modes differ) and modal force coherence.

3.3 Modal disparity

One basic question in the study of close modes is

'How close is close?'

Equation (3) reveals that for ID uncertainty the fundamental definition that measures the difference of modes in an overall sense is $d_i = \sqrt{c_i^2 + e_i^2}$, where $e_i = (f_j - f_i)/f_i\zeta_i$ and $c_i = (f_j\zeta_j - f_i\zeta_i)/f_i\zeta_i$ reflect the difference in frequencies and damping ratios, respectively. 'Disparity' is used as a new term in this work to describe these parameters as they are not simple difference of modal properties. The parameter e_i is often used to measure the difference in frequencies, e.g., $e_1 = 1$ if the frequency of Mode 2 is at the half-power frequency of Mode 1. The presence of c_i reminds that the difference in damping ratios does make the modes different. For close modes it is approximately the fractional difference between the damping ratios, i.e., $c_i \approx (\zeta_j - \zeta_i)/\zeta_i$ because $f_i \approx f_j$. Strictly speaking $c_i \neq 0$ even when $\zeta_1 = \zeta_2$ but in this case $c_i = (f_j - f_i)/f_i << e_i$ and so $d_i \approx e_i$. The theory shows that Pythagoras theorem applies to encapsulate the effect of difference in frequencies and damping ratios in d_i on ID uncertainty, which is a nice result but hardly trivial.

Figure 4 illustrates how two modes with different disparities may appear by plotting their dynamic amplification factors (between modal force and modal acceleration), assuming identical damping ratios. These plots are akin to PSDs of ambient data. They suggest that a disparity of the order of 1 may be considered close while a disparity of 10 is clearly well-separated. A disparity of 0.5 is considered very close. It does happen in field cases; see Table 3 later.
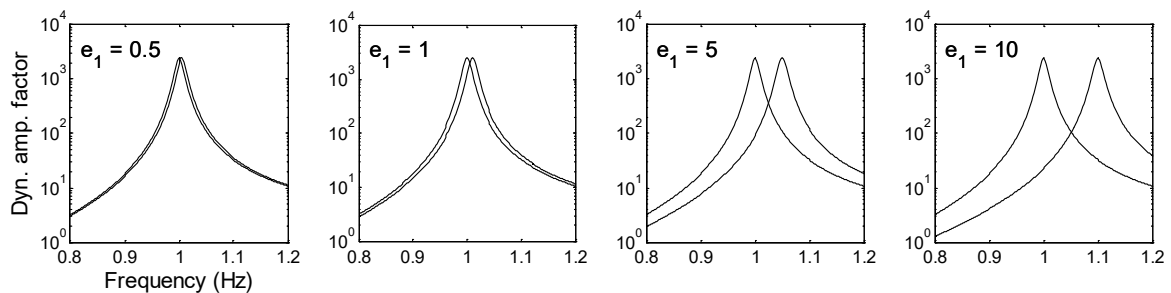
Figure 4 Dynamic amplification factors of two modes with different frequency disparities e_1 of 0.5 (very close), 1 (close), 5 (separated) and 10 (well-separated). The two modes have the same damping (1%) and so $d_i \approx e_i$

As a note, it may appear from (3) that decreasing damping increases $\delta''_{\phi i}$ but this implicitly assumes that d_i is constant. In fact, $d_i^2 \propto 1/\zeta_i^2$ and so $\delta''^2_{\phi i} \propto \zeta_i$, the same for well-separated modes (Type 1 uncertainty). Intuitively, decreasing damping increases the modal s/n ratio and frequency disparity, which reduces Type 1 and Type 2 mode shape uncertainties, respectively.

3.4 Coherence of modal forces

The coherence χ between modal forces is their correlation in the frequency domain. From first principles, if the modal force coherence is zero then the FFTs of the two modal responses will be uncorrelated. Modal force coherence mixes with the disparity parameters to affect the ID uncertainty of all modal properties in a non-trivial manner through the coherence factors $Q_{\phi i}$, Q_{f_i} and Q_{ζ_i} in (4), (10) and (11), respectively. Clearly, the coherence factors are all equal to 1 (no amplification) when $\chi = 0$. The coherence factors depend primarily on $|\chi|$ and modal entangling factors q_i. Through the terms $q_i^2 |\chi|^2$ and $q_i^2 |\chi|^4$ in the expressions of coherence factors, q_i may be seen as discounting the effect of χ on uncertainty amplification; the lower the $|q_i|$ the higher the discount. The value of q_i depends on disparity (e_i, c_i) through another two modal entangling factors g_i in (6), though in a somewhat non-trivial manner.

3.4.1 Bounds on coherence factors

For mode shapes, if $q_1 = q_2$ then the coherence factor $Q_{\phi i} = 1/(1 - q_2^2 |\chi|^2)$ **is monotonically increasing with $|\chi|$** but otherwise this is generally not the case. It is shown in Section 10 (appendix) that

$$0 \le q_1^2 \le q_2^2 \le 1 \tag{17}$$

$$1 \le \frac{1}{1 - q_1^2 |\chi|^4} \le Q_{\phi i} \le \frac{1}{1 - q_2^2 |\chi|^2} \le \frac{1}{1 - |\chi|^2} \tag{18}$$

The lower bound of 1 implies that modal force coherence χ always amplifies Type 2 mode shape uncertainty. For frequencies and damping ratios, the coherence factors Q_{f_i} and Q_{ζ_i} in (10) and

(11) also depend on the phase angles ψ, ϕ and ϕ_i through the factors R_{f_i} and R_{ζ_i} in (12) and

(13). Such dependence is trigonometric in nature and is of less significance than those on q_2 and

$|\chi|$. It is shown in Section 11 (appendix) that

$$0 \le R_{x_i} \le (1 - q_2^2 \,|\chi|^4)[1 - q_2^2 \,|\chi|^2 + q_2^2(1 - |\chi|^2)] \qquad\qquad x = f, \zeta \qquad\qquad (19)$$

Substituting into (10) or (11), and simplifying gives

$$\frac{1 - |\chi|^2}{1 - q_2^2 \,|\chi|^4} \le Q_{x_i} \le \frac{1}{1 - q_2^2 \,|\chi|^2} \qquad\qquad x = f, \zeta \qquad\qquad (20)$$

Simpler (but looser) bounds that depend only on $|\chi|$ can be obtained by further taking $q_2 = 0$ on

the lower bound and $q_2 = 1$ on the upper bound:

$$1 - |\chi|^2 \le Q_{x_i} \le \frac{1}{1 - |\chi|^2} \qquad\qquad x = f, \zeta \qquad\qquad (21)$$

These bounds are plotted in Figure 5. It is useful to note that the c.o.v.s of frequencies, damping

ratios and mode shapes (Type 2) all have the same upper bound of $1/\sqrt{1 - |\chi|^2}$. This implies that

during ambient test planning the effect of coherence on these parameters can be conservatively

treated in the same manner, i.e., with their c.o.v. amplified by $1/\sqrt{1 - |\chi|^2}$. See Section 6 later. The

bounds are illustrated later in Figure 10(e) with synthetic data; Figure 12(e) with laboratory data;

and Figure 14(e), Figure 16(e), Figure 18(e) and Figure 20(e) with field data.
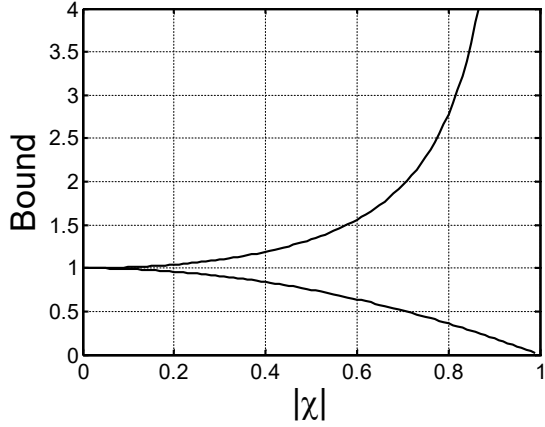
Figure 5 Lower bound ($1-|\chi|^2$) and upper bound ($(1-|\chi|^2)^{-1}$) of coherence factors Q_{f_i} and Q_{ζ_i} in (21); Q_{φ_i} share the same upper bound but it is bounded below by 1, see (18).
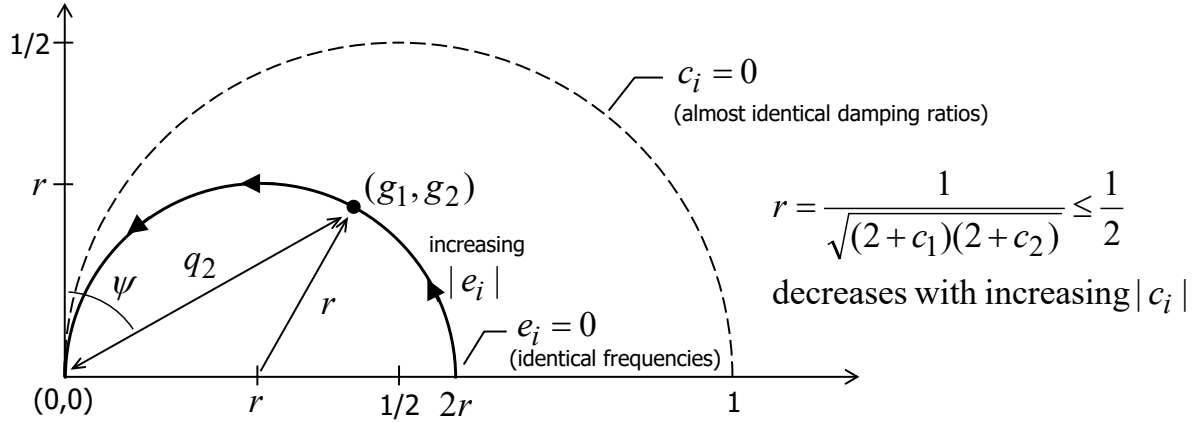
3.4.2 Effect of disparity on modal entangling factors q_i

The effect of disparity parameters (e_i, c_i) on the modal entangling factors q_i is obscured by their relationship with another two entangling factors g_i in (6), on which q_i in (5) depends. Generally, increasing disparity reduces the magnitude of q_i and hence the influence of coherence, which is intuitively correct. It can be shown by direct algebra that the following identity holds:

$$(g_1 - r)^2 + g_2^2 = r^2 \qquad\qquad r = \frac{1}{\sqrt{(2+c_1)(2+c_2)}} \qquad\qquad (22)$$

Figure 6 gives a geometric interpretation of this identity that allows one to see the effect of disparity on q_2. The point (g_1, g_2) always lie on the semi-circle centred at $(r, 0)$ with radius r, as indicated by solid line in the figure. Its distance from the origin is equal to q_2 and the angle it makes with the vertical axis is ψ; see (5). The value of q_1 involves the phase angle ϕ of coherence as well but its magnitude is always bounded above by q_2. For given c_i (hence r), when $e_i = 0$ (identical frequencies), the point is at $(2r, 0)$. As $|e_i|$ increases the point traces along the semi-circle in an anti-clockwise manner as indicated by the arrows. The radius r decreases as $|c_i|$ increases. The semi-circle has a maximum radius of 1/2 when $c_i = 0$ (identical damping ratios), as indicated by dashed line.

Figure 6 Geometric interpretation of the effect of disparity on modal entangling factors g_1, g_2
and q_2 **in (5). Note that** $q_1 = q_2 \sin(2\phi - \psi)$ **and so its value is bounded above by** q_2

3.5 MAC effect

From first glance the effect of MAC ρ on ID uncertainty is somewhat counter-intuitive. Equation (8)
and (9) say that it does not affect the c.o.v.s of frequency and damping ratio; and (3) says that a
higher MAC leads to a lower Type 2 mode shape c.o.v.. The former can be reconciled by noting that
(3), (8) and (9) only give the leading order uncertainty. Further evidence reveals that the first order

uncertainty does deteriorate with increased MAC through a s/n ratio discounted by $(1 - \rho^2)$; see
(26) and Table 1 in Section 4 later. On the other hand, a higher MAC means that the two mode
shapes are closer to each other, which means that there is a lesser extent to which they can 'trade'
(by rotating towards one another) to 'fit' data (give similar likelihood), and hence smaller uncertainty.
Note that the case $\rho = 1$ is excluded from discussion because then the problem degenerates and
the present theory does not apply.

3.6 Zero disparity and mode shape identifiability

One important implication from the uncertainty law is that the c.o.v.s of frequency and damping
ratios in (8) and (9) remain bounded even for two modes with identical frequencies and damping
ratios ($d_i = 0$), suggesting that they are still identifiable. The same is not true for the mode shape
c.o.v. (Type 2) in (3), however. To have a better understanding of this issue, note that when $d_i = 0$
the FRFs of the two modes are identical, i.e., $h_{1k} \equiv h_{2k}$, and so the scaled FFT of data becomes

$$\mathcal{F}_k = \varphi_1 h_{1k} p_{1k} + \varphi_2 h_{2k} p_{2k} + \xi_k = \Phi \mathbf{p}_k h_{1k} + \xi_k \qquad\qquad (f_1 = f_2, \; \zeta_1 = \zeta_2) \qquad (23)$$

where $\mathbf{\Phi}=[\boldsymbol{\varphi}_1,\boldsymbol{\varphi}_2]$ ($n \times 2$ real partial mode shape matrix) and $\mathbf{p}_k=[p_{1k},p_{2k}]^T$ (2×1 complex vector of modal forces) is the scaled FFT of modal forces and $\boldsymbol{\xi}_k$ is the scaled FFT of noise. The FRF h_{1k} carries information about frequencies and damping ratios. The presence of the FRF in (23) allows them to be identified even when $d_i = 0$. The term $\mathbf{\Phi}\mathbf{p}_k$ carries information about mode shapes and modal force PSDs. The following shows that they are unidentifiable. Generally, we can write $\mathbf{p}_k$ as a linear transformation of another random scaled FFT vector $\mathbf{z}_k$ of the same dimension, i.e., $\mathbf{p}_k = \mathbf{T}\mathbf{z}_k$, where $\mathbf{T}$ is a real invertible matrix and the PSD matrix of $\mathbf{z}_k$ is $\mathbf{S}_z = \mathbf{T}^{-1}\mathbf{S}\mathbf{T}^{-T}$ so that the PSD matrix of $\mathbf{p}_k$ is preserved:

$$E[\mathbf{p}_k\mathbf{p}_k^*] = \mathbf{T}E[\mathbf{z}_k\mathbf{z}_k^*]\mathbf{T}^T = \mathbf{T}\mathbf{S}_z\mathbf{T}^T = \mathbf{T}(\mathbf{T}^{-1}\mathbf{S}\mathbf{T}^{-T})\mathbf{T}^T = \mathbf{S} \tag{24}$$

Substituting $\mathbf{p}_k = \mathbf{T}\mathbf{z}_k$ into (23) gives $\mathcal{F}_k = (\mathbf{\Phi}\mathbf{T})\mathbf{z}_k h_{1k} + \boldsymbol{\xi}_k$, which implies a modal force vector of $\mathbf{z}_k$ and a mode shape matrix of $\mathbf{\Phi}\mathbf{T}$ whose columns are linear combinations of $\boldsymbol{\varphi}_1$ and $\boldsymbol{\varphi}_2$. In the above argument, $\mathbf{T}$ is arbitrary and this implies that the mode shapes and modal force PSD matrix are not identifiable. Since the columns of $\mathbf{\Phi}\mathbf{T}$ are linear combinations of those of $\mathbf{\Phi}$ with the same number of linearly independent columns ($\mathbf{T}$ is invertible), the space spanned by the mode shapes, i.e., mode shape subspace, can still be identified. These conclusions can also be reached by examining the PSD matrix of data, which is the only term in the likelihood function for modal ID that depends on modal parameters. When $d_i = 0$,

$$\begin{aligned}\mathbf{E}_k &= \mathbf{\Phi}\,diag\{h_{1k},h_{2k}\}\ \mathbf{S}\ diag\{h_{1k},h_{2k}\}^*\mathbf{\Phi}^T + S_e\mathbf{I}_n \\ &= \mathbf{\Phi}\mathbf{S}\mathbf{\Phi}^T \mid h_{1k}\mid^2 + S_e\mathbf{I}_n\end{aligned} \qquad (f_1 = f_2,\ \zeta_1 = \zeta_2) \tag{25}$$

Again, $\mid h_{1k}\mid^2$ provides the information for identifying the frequencies and damping ratios. The matrix $\mathbf{\Phi}\mathbf{S}\mathbf{\Phi}^T$ can be written as $(\mathbf{\Phi}\mathbf{T})(\mathbf{T}^{-1}\mathbf{S}\mathbf{T}^{-T})(\mathbf{\Phi}\mathbf{T})^T$ for arbitrary real invertible $\mathbf{T}$, which corresponds to a mode shape matrix of $\mathbf{\Phi}\mathbf{T}$ and modal force PSD matrix of $(\mathbf{T}^{-1}\mathbf{S}\mathbf{T}^{-T})$, showing again that they are not identifiable.

The ideal scenario of zero disparity is discussed here to illustrate identifiability, although it is almost impossible in reality because it is very sensitive to structural configuration. Equation (3) shows that as long as disparity is non-zero it is still possible to identify mode shapes but the required data

length can be significantly longer than that for well-separated modes when disparity is small (even for noiseless data). This governs the achievable identification precision of close modes. It should be noted that the issue of disparity discussed here is related to the temporal/frequency rather than spatial aspect of response/data. It does not have a direct linkage with observability that is often discussed in the system identification literature.

4   Bandwidth and s/n ratio effect

The results in Section 2 assume that the resonance band for modal ID is sufficiently wide, in the sense that $\kappa \gg 1$ and $\kappa \gg e_i$. In the development of theory it was found necessary to introduce this assumption in order to obtain rigorously the closed form asymptotic expressions for c.o.v.s with reasonable simplicity as presented in the section. On other hand, the expressions capture only the leading order of the c.o.v.s which turn out to be independent of the noise PSD S_e and hence s/n ratio, except for Type 1 mode shape uncertainty which is nevertheless negligible for high s/n ratio. Finite bandwidth and s/n ratio encountered in reality do make a difference to ID uncertainty especially when they are not wide/high. Addressing these two issues in a mathematically rigorous manner is another challenge that is left for the future. In this work, 'correction factors' A_κ and A_γ in Table 1 are proposed empirically based on the wide-band theory and numerical investigation to capture the effect of bandwidth and s/n ratio, respectively. The c.o.v. of a parameter is equal to the value in Section 2 multiplied by A_κ and A_γ.

Table 1 Empirical correction factors A_κ and A_γ to account for bandwidth and s/n ratio effect; mode number is omitted for notational simplicity

c.o.v.	$\mathbf{A}_\kappa$	$\mathbf{A}_\gamma$
Frequency c.o.v. δ_f	$\left[\dfrac{2}{\pi}(\tan^{-1}\kappa - \dfrac{\kappa}{\kappa^2+1})\right]^{-1/2}$	$\sqrt{1+\dfrac{a_f}{\gamma''}}$
Damping c.o.v. δ_ζ	$\left[\dfrac{2}{\pi}\left(\tan^{-1}\kappa + \dfrac{\kappa}{\kappa^2+1} - \dfrac{2(\tan^{-1}\kappa)^2}{\kappa}\right)\right]^{-1/2}$	$\sqrt{1+\dfrac{a_\zeta}{\gamma''}}$
Mode shape c.o.v. (Type 1) δ'_φ	$\left[\dfrac{2}{\pi}\tan^{-1}\kappa\right]^{-1/2}$	1
Mode shape c.o.v. (Type 2) δ''_φ	$\left[\dfrac{2}{\pi}(\tan^{-1}\kappa)\left(1-\dfrac{\tan^{-1}\kappa}{\kappa}\right)\right]^{-1/2}$	$\sqrt{1+\dfrac{a_\zeta}{\gamma''}}$

In Table 1,

$$\kappa = \frac{\text{bandwidth (Hz)}}{2f\zeta} \qquad\qquad \gamma'' = \underbrace{\frac{S}{4S_e\zeta^2}}_{\gamma'}(1-\rho^2)(1-|\chi|^2) \qquad (26)$$

are respectively the bandwidth factor and modal s/n ratio for the subject mode with natural frequency f, damping ratio ζ and modal force PSD S (mode index omitted for simplicity); and

$$a_f = \frac{4(\kappa - \tan^{-1}\kappa)}{\tan^{-1}\kappa - \dfrac{\kappa}{\kappa^2+1}} \qquad a_\zeta = \frac{4(\kappa^2+1)(3\tan^{-1}\kappa - 3\kappa + \kappa^2\tan^{-1}\kappa)\tan^{-1}\kappa}{3[(\kappa^2+1)(\kappa - 2\tan^{-1}\kappa)\tan^{-1}\kappa + \kappa^2]} \qquad (27)$$

For δ_f, δ_ζ and δ'_φ, the expressions of A_κ are the same as their counterparts for well-separated modes [39]. For δ''_φ, the expression of A_κ is proposed based on observations during development of the wide band theory. The expressions of A_γ are based on their counterparts for well-separated modes, except for δ'_φ that already contains s/n effect and hence does not need to be further corrected. The s/n ratio γ'' in (26) is different from γ'_i in (2). The latter is the familiar one for well-separated modes. For close modes, γ'' is more intrinsic to capture the effect of s/n ratio. It is motivated from the first order term in the Taylor expansion of the inverse of the data PSD matrix; see equation (9) of [41]. The factors $(1-\rho^2)$ and $(1-|\chi|^2)$ in γ'' discount the amount of information in data for higher MAC or modal force coherence, which is intuitive.

To illustrate the quality of approximation based on the empirical correction factors, consider two modes with frequencies $f_1 = 1$ Hz and $f_2 = 1.01$ Hz, damping ratios $\zeta_1 = 1\%$ and $\zeta_2 = 1.5\%$, and modal force PSDs $S_{11} = 2(\mu g)^2/Hz$ and $S_{22} = 3(\mu g)^2/Hz$. Modal force coherence $\chi = S_{21}/\sqrt{S_{11}S_{22}}$ has a modulus of $|\chi| = 0.5$ and its phase angle will be varied in the study. The (partial) mode shapes are taken to be

$$\varphi_1 = \frac{1}{\sqrt{5+x^2}}\begin{bmatrix} 1 \\ 2 \\ x \end{bmatrix} \qquad\qquad \varphi_2 = \frac{1}{\sqrt{5+x^2}}\begin{bmatrix} -2 \\ 1 \\ x \end{bmatrix} \qquad\qquad x = \sqrt{\frac{5\rho}{1-\rho}} \qquad (28)$$

Check that these mode shapes have unit norm and their MAC is ρ, which is set to be 0.5. The data

has a duration of 1000 sec and a high s/n ratio of $\gamma'' = 10^4$. Figure 7 shows the values (cross) based

on the empirical correction factors in Table 1 versus the 'exact' values based on the inverse of the

exact form of Fisher Information Matrix (FIM) evaluated at the 'true' parameter values assumed

here, i.e., (14). The latter involves no assumption on bandwidth or s/n ratio, although it does not

yield any insight because of its implicit form. The high s/n ratio and wide band asymptotic values

(blue dots) are also shown for comparison. They are based on (1), (8) and (9) in Section 2. The points

in the figure correspond to two modes identified with bandwidths $\kappa = 5,6,...,20$; and ten values of

phase angles ϕ of modal force coherence ($\chi = |\chi| e^{\mathbf{i}\phi}$) spanning uniformly from 0 to 2π. As the

bandwidth increases the blue dots go from the right to left without shifting vertically because their y

axis values have not accounted for bandwidth. After modification with empirical correction factors,

the crosses scatter along the 1:1 line, demonstrating capability to capture bandwidth effect. Figure 8

is analogous to Figure 7 except now the s/n ratio γ'' spans from 10, 20,…, to 1000, 2000, …, 10^4 ;

while the bandwidth is set at $\kappa = \min(2\sqrt{\gamma''},10)$ to reflect the narrowing of usable bandwidth due

to reduced s/n ratio when it is small [39]. Again, the scattering of crosses around the 1:1 line

demonstrate some capability of capturing s/n ratio effect. The results for $\rho = 0.5$ and $|\chi| = 0.5$ are

presented here as they are considered to be representative of typical cases. Further numerical

results (omitted here) reveal that the quality of approximation is similar for other values of ρ but

tends to worsen (greater scatter) as $|\chi|$ increases.
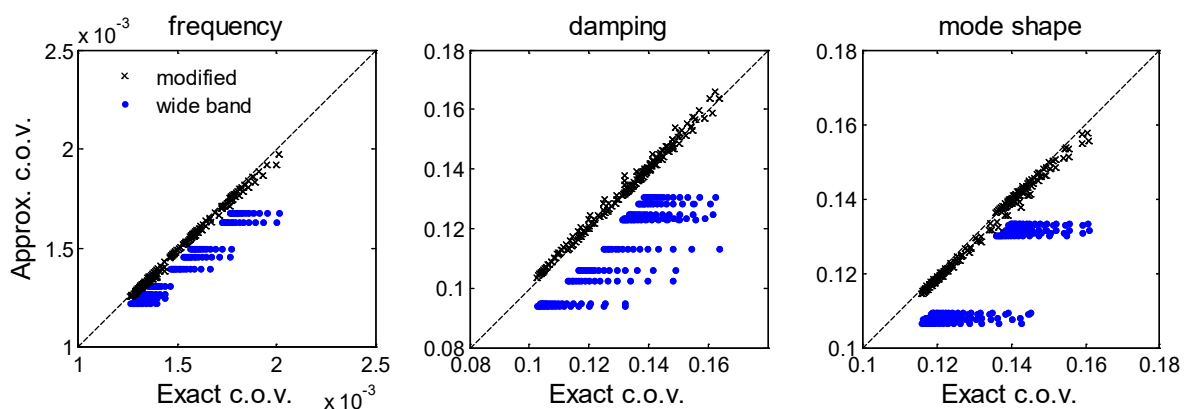
Figure 7 Capture of bandwidth effect by empirical correction factor; exact value is based on inverse of exact FIM (see (14)); wide band value is based on (1), (8) and (9); empirically corrected value is wide band value multiplied by A_κ and A_γ. Results for the two modes are not distinguished
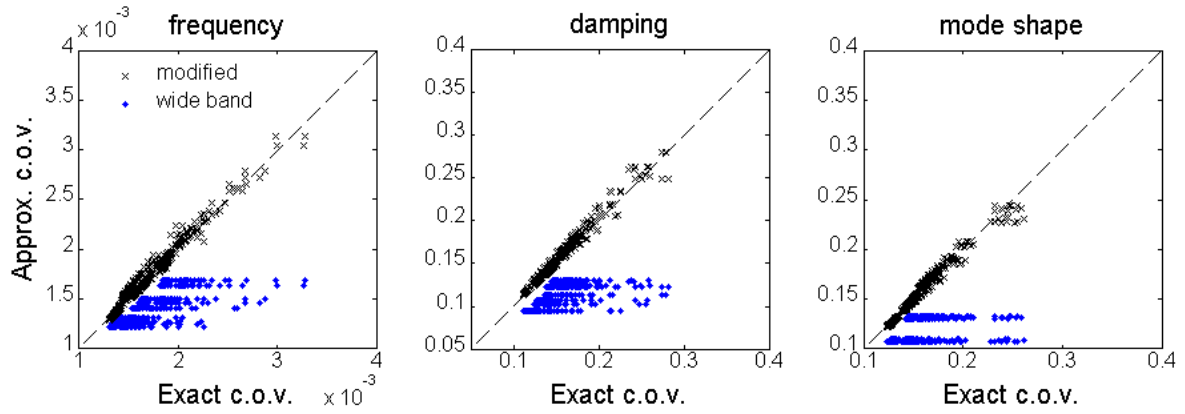
Figure 8 Capture of s/n ratio effect by empirical correction factor; exact value is based on inverse of exact FIM (see (14)); wide band value is based on (1), (8) and (9); empirically corrected value is wide band value multiplied by A_κ and A_γ. Results for the two modes are not distinguished

5   Verification and applications

In this section the uncertainty law of close modes developed in this work is investigated with synthetic, laboratory and field data. Six cases are considered and summarised in Table 2; see also Figure 9. In each case multiple data sets are analysed. The case with synthetic data has the same first mode properties and mode shapes as in the example in Section 4, but other properties are varied to cover a wide range of scenarios. It aims at verifying the mathematical correctness of the wide band expressions (1), (8) and (9) in Section 2. It also illustrates what the results will be like in an ideal situation without modelling error. The other cases with experimental data investigate the quality of the wide band expression combined with the empirical correction factors in Table 1 in the real setting. They also allow us to develop insights into the mechanism that gives rise to the ID uncertainty by investigating the statistics of governing factors. Laboratory data was collected with piezoelectric accelerometers with channel noise in the order of 10 micro-$g/\sqrt{Hz}$. Field data was collected with servo-accelerometers with channel noise in the order of 1 micro- $g/\sqrt{Hz}$.

Table 2 Summary of investigated cases

Structure	Data duration	Measured DOFs	Remark
Synthetic data	1000 sec/set x 100 set at 10Hz	3 DOFs	$f_1 = 1\text{Hz Hz}$, $\zeta_1 = 1\%$
			$S_{11} = 2(\mu g)^2 / \text{Hz}$, $S_e = 0.1(\mu g)^2 / \text{Hz}$
			Other properties randomised uniformly:
			f_2 on 1-1.1Hz, ζ_2 on 0.5%-5%
			S_{22} on 2-4 $(\mu g)^2 / \text{Hz}$
			φ_1 and φ_2 from (28) with ρ on 0-1
			$\chi = \mid \chi \mid e^{\mathbf{i}\phi}$ with

			$\lvert \chi \rvert$ on 0-1 and ϕ on 0 - 2π
			Resulting $\kappa = 10 - 20+$, s/n ratio = $1000 - 10^4+$
			Figure 10
Lab model	600 sec/set x 54 set = 3 h at 256Hz	4 DOFs, xy at two corners on long side of top floor	3-storey shear frame, 5kg per floor, wide bandwidth, low to high s/n ratio with electric fan at different distances
			$\kappa = 2 - 20$, s/n ratio = $10 - 10^4+$
			Figure 11 and Figure 12
Building B in [12]	30 min./set x 72 set = 36 h at 50Hz	3 DOFs, xyz near core on roof; see Fig.3(b) in [11]	300m+ tall commercial building, very close modes, during typhoon, low to high amplitude
			$\kappa = 2 - 20+$, s/n ratio = $50 - 10^4+$
			Figure 13 and Figure 14
Eddystone Lighthouse [18]	10 min./set x 60 sets = 10 h at 128Hz	4 DOFs, xy at two levels between 1/2 and 2/3 height; see Fig.8 in [18]	49m tower, Helipad acts like a TMD, complicated wind/seawave environment
			$\kappa = 5 - 20$, s/n ratio = $200 - 10^4+$
			Figure 15 and Figure 16
Jiangyin Bridge [44]	3200sec/set x 13 sets = 11.6h at 25.6Hz	4 DOFs, transverse & vertical at two ref. locations near 1/4 span; see Fig.13 in [44]	Long span suspension bridge, 1.4km main span, under normal traffic,
			$\kappa = 2 - 10$, s/n ratio = $50 - 4000$
			Figure 17 and Figure 18
Rugeley Chimney [16]	1200sec/set x 138 sets = 46h at 8Hz	4 DOFs, xy (radial and tangential) at two levels, near top and 1/4 height; see Fig.3 in [16]	183m chimney with TMD, under normal wind condition, apparently significant deviation from classical damping
			$\kappa = 3 - 20+$, s/n ratio = $1000 - 10^4+$
			Figure 19 and Figure 20

| Lab shear frame | Jiangyin Yangtze Bridge | Eddystone lighthouse | Rugeley Chimney |
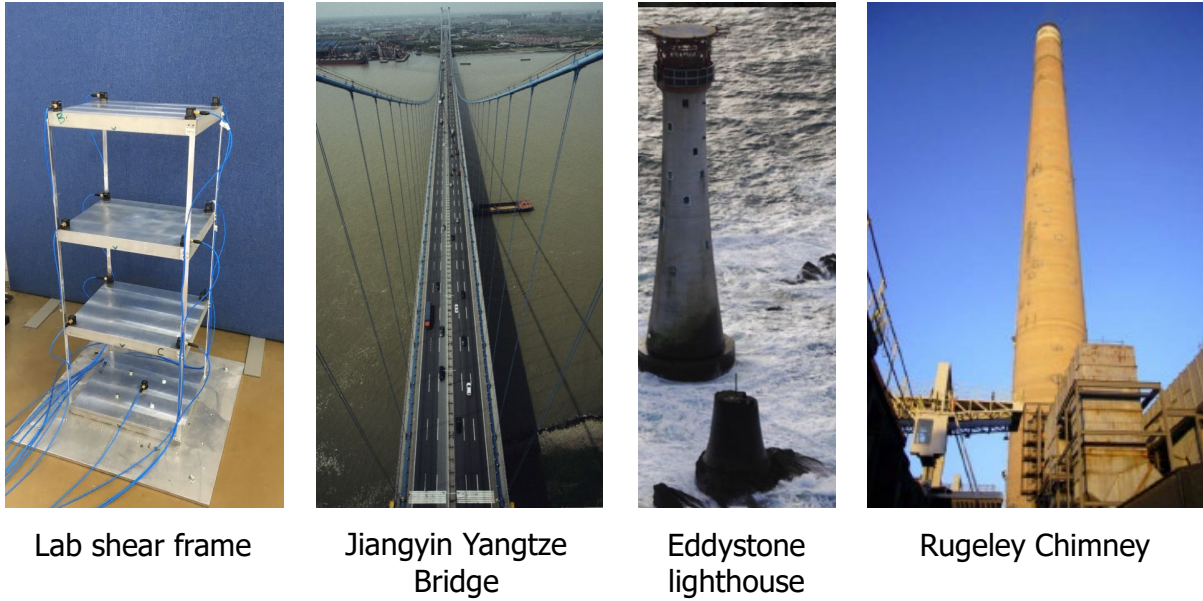
**Figure 9 Some structures considered in the study**

5.1 Synthetic data

The synthetic data features a moderately high s/n ratio (>1000), wide band ($\kappa > 10$) and long data (about 1000 natural periods in each set). One hundred data sets with different modal properties are randomly generated to cover a variety of scenarios. Figure 10(a)-(c) show the c.o.v.s of frequencies, damping ratios and mode shapes. Recall that the mode shape c.o.v. is defined as the square root sum of eigenvalues of the mode shape posterior covariance matrix. For small value, it can be interpreted as the expected hyper-angle between the uncertain mode shape and its MPV. The x-axis shows the values calculated by Bayesian modal ID algorithm (BAYOMA) [28] for each data set. This is the value one uses in applications for assessing ID uncertainty conditional on the particular data set when it is available; but the point-wise value does not explain the calculated uncertainty. In BAYOMA, the most probable value (MPV) of modal parameters is first calculated by minimising the negative log of the likelihood function (NLLF). The posterior covariance matrix of modal parameters is then calculated as the inverse of the Hessian of NLLF evaluated at the MPV. Each diagonal entry of this matrix gives the corresponding posterior variance of the parameter, which subsequently gives the c.o.v. (= square root of variance/MPV) that is plotted on the x-axis.

In Figure 10(a)-(c), the y-axis shows the uncertainty law values developed based on different contexts, which try to explain the BAYOMA values along the x-axis. The green dots show the values assuming well-separated modes [39]. They are far away from the 1:1 (dashed) line, indicating that they cannot capture the behaviour of ID uncertainty for close modes especially for mode shape

uncertainty. The red circles show the values based on the inverse of the exact Fisher Information Matrix (FIM); see Section 3.1 and (14). Being a theoretical ensemble average over long data in hypothetical repeated experiments distributed according to the same likelihood function of BAYOMA, the exact FIM (or uncertainty law) value does not depend on the particular data set used but rather the 'true' modal properties (which is assumed to exist). Although the latter is known in this synthetic data example, it is not known (in fact, does not exist) in general applications with experimental data. To be consistent with the general context, when calculating the exact FIM (or uncertainty law) value the true parameter value is substituted by the most probable value (MPV) calculated by BAYOMA based on the particular data set. Statistically significant deviation of the exact FIM values (red circles) from the 1:1 line is an indication of modelling error for that particular data set. For its semi-analytical nature, the exact FIM can be considered as one step towards explaining ID uncertainty. Nevertheless its implicit nature (e.g., still in terms of matrices) does not yet allow direct insights to be developed. This ultimate goal is addressed by the uncertainty law developed, i.e., wide band expressions ((1), (8) and (9)) modified by the factors in Table 1 to account for finite bandwidth and s/n ratio. Their values are shown as crosses ('x') in Figure 10(a)-(c). They represent the best effort of this work to explain the ID uncertainty of close modes. They agree with the red circles, effectively verifying the mathematical correctness of the wide band law.

As a remark, if the data used is long and it is indeed distributed as the same likelihood function as in BAYOMA/FIM, i.e., no modelling error (as is possible for synthetic data here), the BAYOMA value (x-axis) will theoretically converge (in a statistical sense) to the exact FIM value (y-axis, red circle). In this sense the exact FIM value is the closest analytical value one can get to match the BAYOMA value; see [45] for a further discussion. However, this convergence is only a theoretical statement which can at best be expected from synthetic data because no model is perfect for experimental data. This aspect of convergence is only relevant in the verification of mathematical correctness (at the research stage) of the exact FIM or uncertainty law where synthetic data must be used. It is irrelevant to the intended application of uncertainty law, however, which is to understand and manage ID uncertainty for planning tests where no data is available.
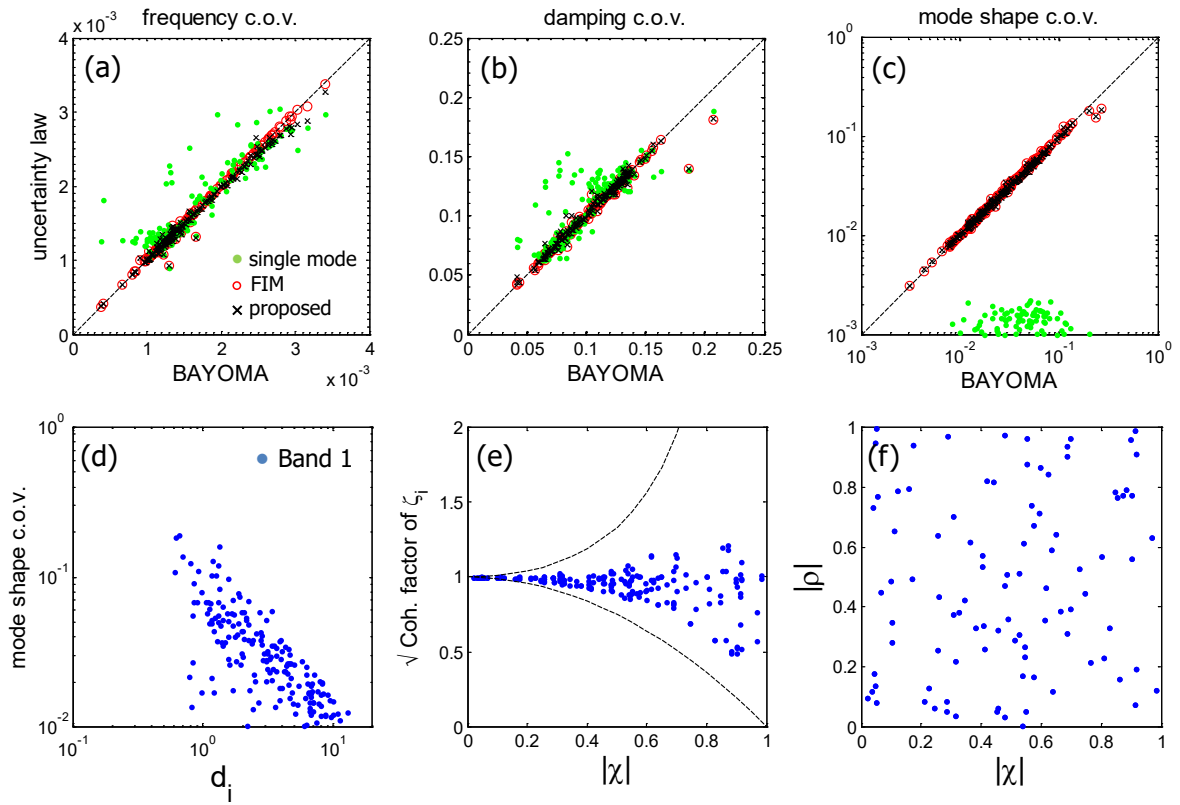
Figure 10 Summary of results, synthetic data. (a), (b) and (c): comparison of c.o.v. from uncertainty laws vs BAYOMA (for given data); green dot – well-separated modes law [39], black cross – close modes law (wide band) corrected with empirical factors, red circle – based on exact FIM (see (14)); (d) mode shape c.o.v. vs disparity d_i; (e) square root of coherence factor of damping vs modulus of coherence $|\chi|$; (f) absolute value of MAC, $|\rho|$, versus modulus of coherence, $|\chi|$

Figure 10(d)-(f) offer some understanding of ID uncertainty based on the proposed uncertainty law (wide band with empirical factors). The values of d_i, $|\chi|$ and ρ are calculated based on the MPVs of modal properties identified from the data sets. Figure 10(d) shows the mode shape c.o.v. versus modal disparity d_i in (7). In all the six cases considered here as well as in typical applications, Type 1 mode shape uncertainty (i.e., orthogonal to both mode shapes; the only type for well-separated modes) is negligible and so the mode shape c.o.v. shown in the plots is effectively of Type 2, i.e., with uncertain directions within the subspace spanned by the two mode shapes. The points exhibit a general decreasing trend, which is consistent with $\delta''_{\varphi_i} \propto 1/d_i$ in (3). The scatter is due to variations in other properties among the data sets, e.g., modal force coherence and MAC.

Figure 10(e) shows $\sqrt{Q_{\zeta_i}}$ in (11), which is the amplification of damping c.o.v. due to modal force coherence χ. The amplification depends on $|\chi|$ and other parameters but it is bounded between $1-|\chi|^2$ and $(1-|\chi|^2)^{-1}$ as in (21). This is demonstrated in the plot. Finally, Figure 10(f) shows the values of $|\chi|$ and ρ (MAC) among the data sets. For the synthetic data sets here they are distributed uniformly merely because of the way they are generated. For the laboratory and field cases later they reflect statistics in the corresponding situations.

5.2 Laboratory and field data

We now discuss the results of the laboratory and field data in a collective manner w.r.t. different aspects. Figure 11, Figure 13, Figure 15, Figure 17 and Figure 19 show the spectra (PSD and SV) of a typical data set in each case. The results analogous to Figure 10 are summarised in Figure 12, Figure 14, Figure 16, Figure 18 and Figure 20.

The cases collectively cover low to high s/n ratios, from a few tens to over ten thousand. The laboratory shear frame is intended to provide an experimental case under controlled environment. Rugeley Chimney provides a case with obvious violation of modelling error, i.e., non-classical damping due to tuned mass damper (TMD). Modal ID of the field structures has been studied previously; see references in the first column of Table 2. The current investigation provides an opportunity to understand their ID uncertainties. The tall building, lighthouse and chimney have close fundamental modes that govern their vibration response, giving compelling reasons for their proper identification and understanding. The lighthouse data is unconventional; obtaining it is a challenge in itself.

On the verification side, in the plots (a)-(c) of Figure 12, Figure 14, Figure 16, Figure 18 and Figure 20, the crosses roughly match with the red circles, suggesting that the proposed formulae (wide band expressions with empirical factors) can give a good match with what can be best achieved (exact FIM). Outliers do exist, e.g., for laboratory frame (one point in Figure 12(c)). The amount of scattering in the crosses and circles about the 1:1 line is similar in all cases except for Rugeley Chimney, which is a special case with modelling error to be discussed later. Similar to the case of synthetic data, the green dots (well-separated modes law) in plot (c) fall below the 1:1 line by orders of magnitude, showing that they fail to explain the ID uncertainty of mode shapes of close modes. They perform better on the frequencies and damping ratios (plots (b) and (c)), typically attaining the right order of magnitude.

Table 3 gives a summary of the statistics of the identified (MPV) damping ratio, disparity, coherence and MAC between the two modes in each band. It can be examined together with plots (d)-(f) in Figure 12, Figure 14, Figure 16, Figure 18 and Figure 20. Damping ratio ranges from 0.5% to a few percent, which is typical. Rugeley Chimney is an exception, with values of 10% for some data sets that can be potentially erroneous because of modelling error (see Section 5.3). The laboratory frame was designed to have identical stiffness along the two horizontal axes, although the ID results indicated that the field structures have even lower disparity. Disparity has a mean value of the order of 1 and a low value around 0.5. Data sets with low disparity are associated with high mode shape c.o.v. and can present challenge for modal ID. See for example the left end of Figure 14(d) for the tall building and Figure 16 for the lighthouse. Coherence and MAC are typically not high, except for a small number of data sets that can give values as high as 0.85, e.g., the tall building. Those are associated with a high mode shape c.o.v., however.

5.3   Effect of modelling error

Uncertainty law is intended to explain ID uncertainty assuming that the data behaves according to modelling assumptions. Logically when there is significant deviation from modelling assumptions it need not serve the intended purpose. Rugeley Chimney had a TMD installed at the top when the data was collected. It provides a case with apparent modelling error regarding classical damping. The PSD and SV spectra in Figure 19 have a hump on the left side of the natural frequencies, which is judged to be attributed to the action of the TMD. The presence and extent of the hump change from one data set to another, presumably as the TMD action changes in direction and extent. Ideally the TMD introduces two additional modes (along two horizontal directions) to the structure but since the DOFs at the TMD are not measured (as is typical), it is often not possible to distinguish the TMD modes. Thus, only the two modes with very close frequencies are identified in the band assuming classical damping (as in BAYOMA). This clearly induces modelling error, although the effect is unknown. The crosses and red circles in Figure 20(a)-(c) have a larger scatter about the 1:1 line than those in the plots (a)-(c) of Figure 12, Figure 14, Figure 16 and Figure 18. This is especially so for the damping ratio and is believed to be associated with modelling error.

Table 3 Summary of statistics for experimental cases. Some low values of disparity and high values of coherence and MAC are highlighted in bold

| Case	Band	Damping ζ_i			Disparity d_i			Coherence $\lvert\chi\rvert$			MAC $\lvert\rho\rvert$		
		Min.	Mean	Max.	Min.	Mean	Max.	Min.	Mean	Max.	Min.	Mean	Max.
Lab frame	1	0.5%	0.7%	1.1%	1.1	2.2	3.8	0.03	0.17	0.38	0.00	0.07	0.23
(Figure 10)	2	0.6%	0.8%	1.0%	1.3	2.0	2.7	0.09	0.23	0.45	0.00	0.21	0.51
	3	0.4%	0.9%	2.0%	1.3	3.7	6.9	0.01	0.20	0.36	0.01	0.11	0.26
Tall building	1	0.3%	1.4%	3.9%	**0.3**	2.1	10	0.03	0.31	**0.82**	0.00	0.24	**0.85**
(Figure 12)	2	0.5%	1.9%	5.1%	0.4	2.7	12	0.01	0.24	0.76	0.01	0.19	0.55
	3	0.5%	1.2%	2.5%	0.4	1.0	2.1	0.00	0.41	**0.81**	0.00	0.29	0.70
Lighthouse	1	1.5%	1.8%	2.2%	0.8	1.0	1.4	0.02	0.12	0.30	0.03	0.24	0.48
(Figure 14)	2	0.3%	0.5%	0.9%	2.1	3.9	6.7	0.00	0.06	0.14	0.00	0.03	0.12
	3	1.0%	1.3%	1.7%	**0.2**	0.5	0.8	0.01	0.19	0.70	0.00	0.22	0.60
Jiangyin Bridge	1	0.5%	0.9%	1.9%	0.5	1.1	2.5	0.04	0.14	0.26	0.04	0.22	0.60
(Figure 16)	2	0.5%	0.8%	1.4%	1.9	3.7	5.6	0.04	0.09	0.13	0.03	0.11	0.22
	3	0.5%	0.9%	1.2%	1.4	1.9	2.7	0.03	0.10	0.19	0.01	0.07	0.22
Rugeley Chimney (Figure 18)	1	0.5%	3.1%	22%	0.6	3.7	25	0.04	0.51	**0.96**	0.00	0.28	0.74
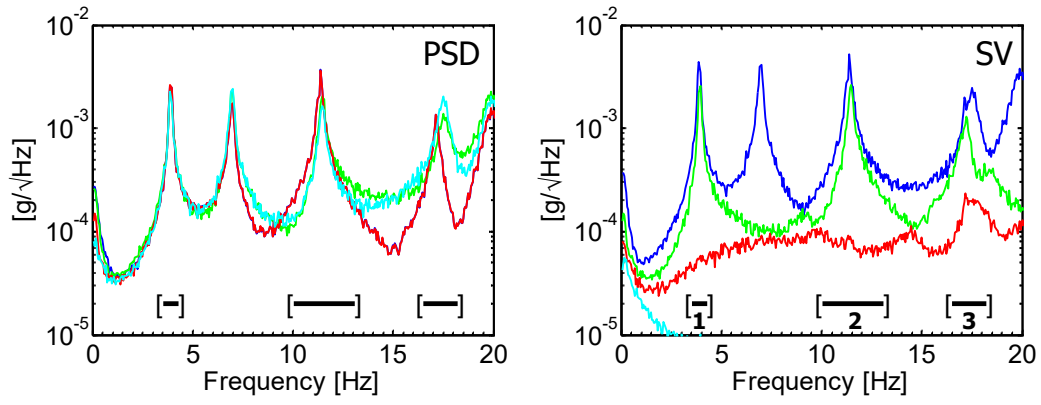
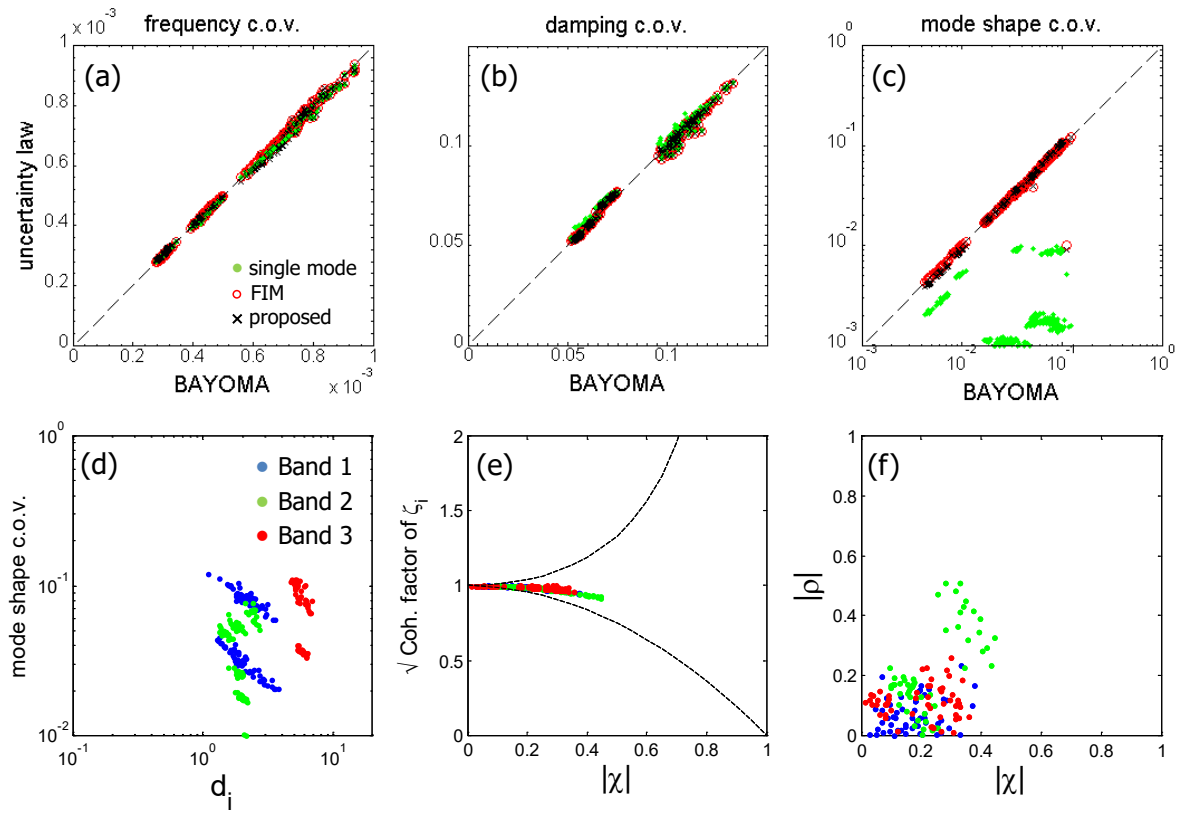**Figure 11 PSD and SV spectra of a typical data set, laboratory shear frame**

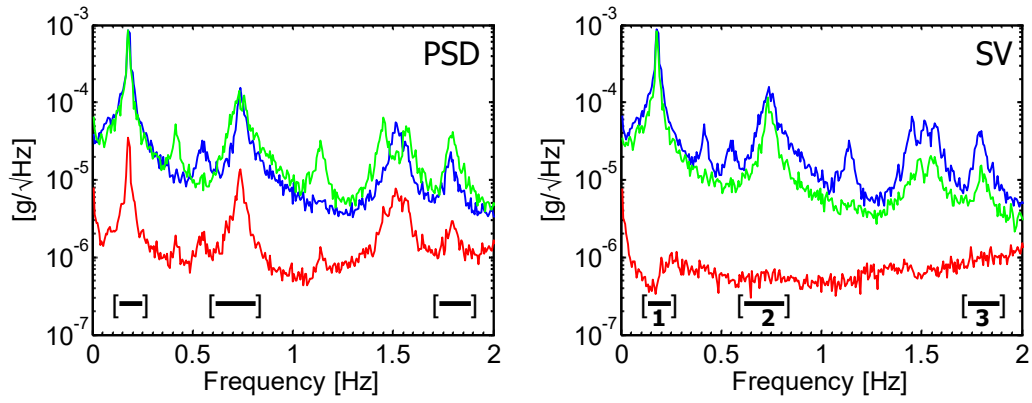**Figure 12 Summary of results, Laboratory shear frame. Same legend as Figure 10**

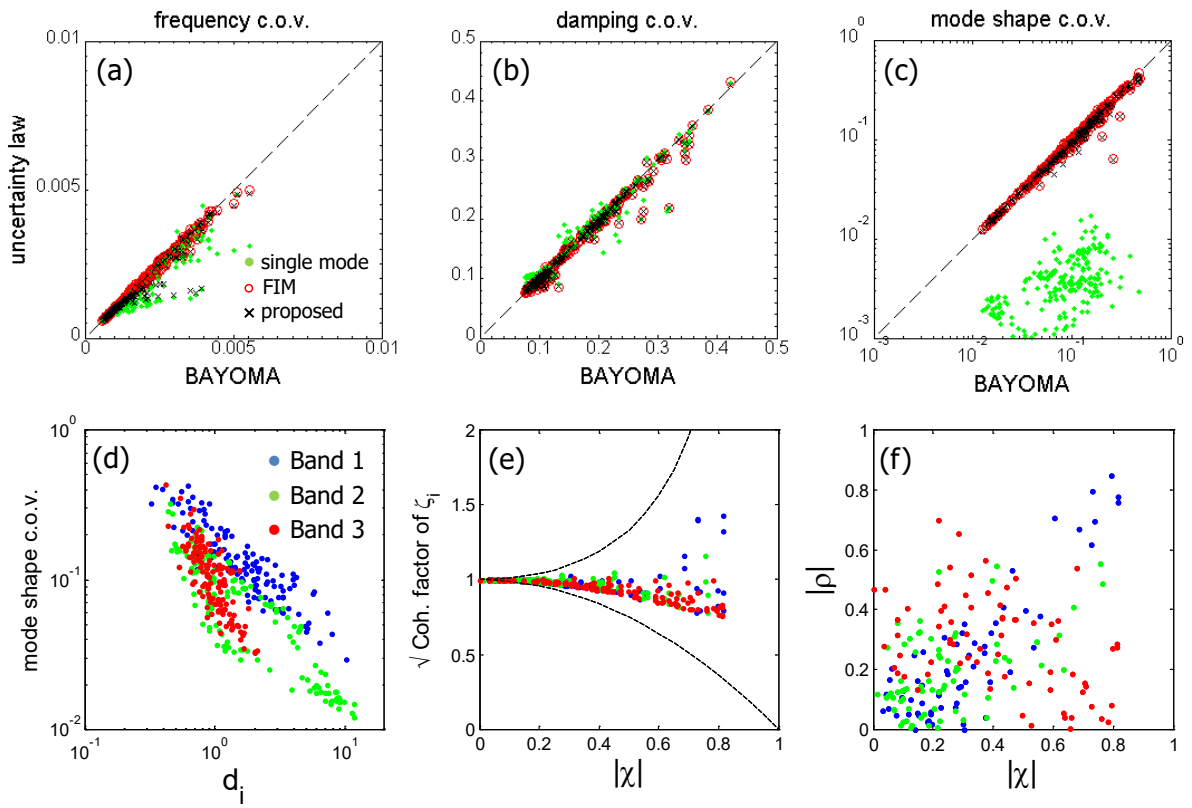**Figure 13 PSD and SV spectra of a typical data set, tall building**

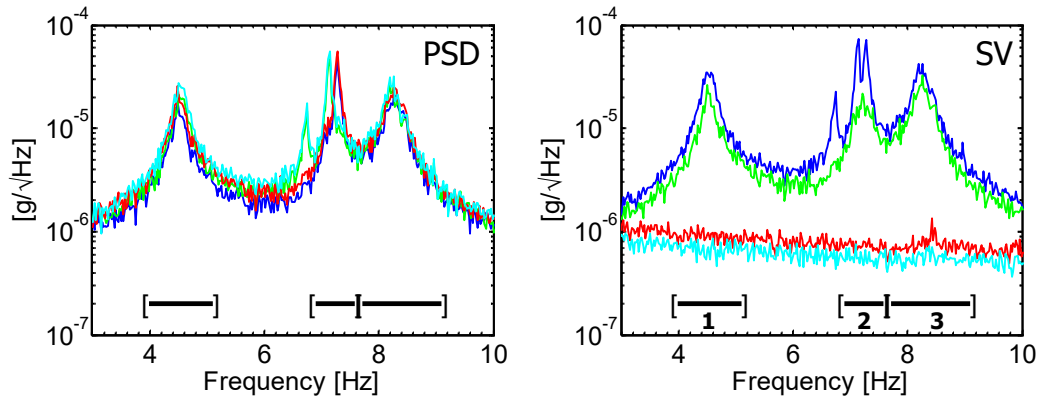**Figure 14 Summary of results, tall building. Same legend as Figure 10**

Figure 15 PSD and SV spectra of a typical data set, Eddystone lighthouse

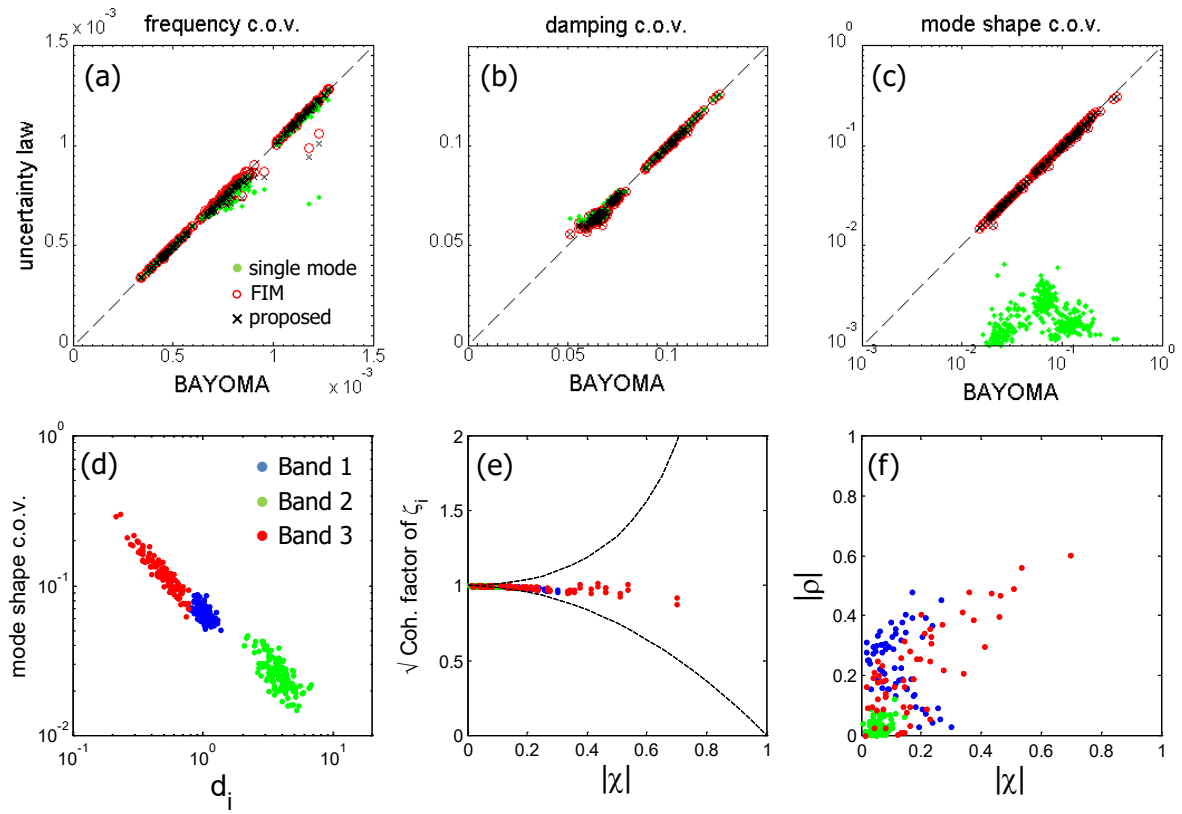

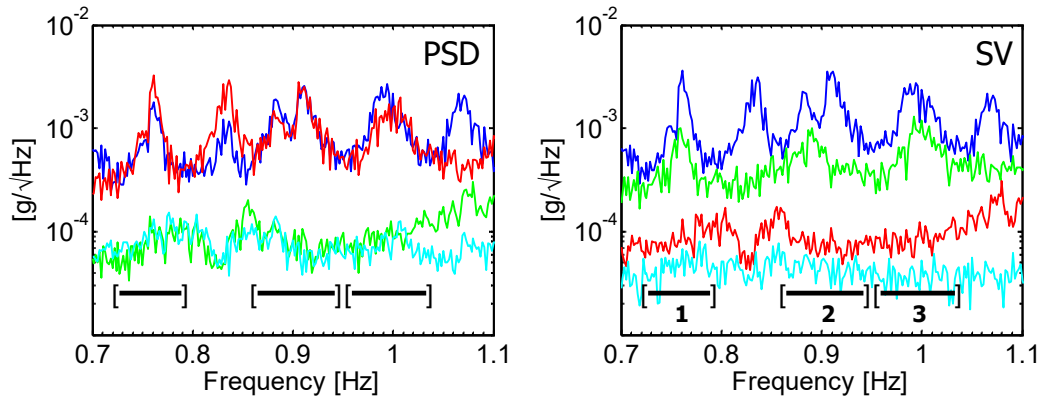**Figure 16 Summary of results, Eddystone lighthouse. Same legend as Figure 10**

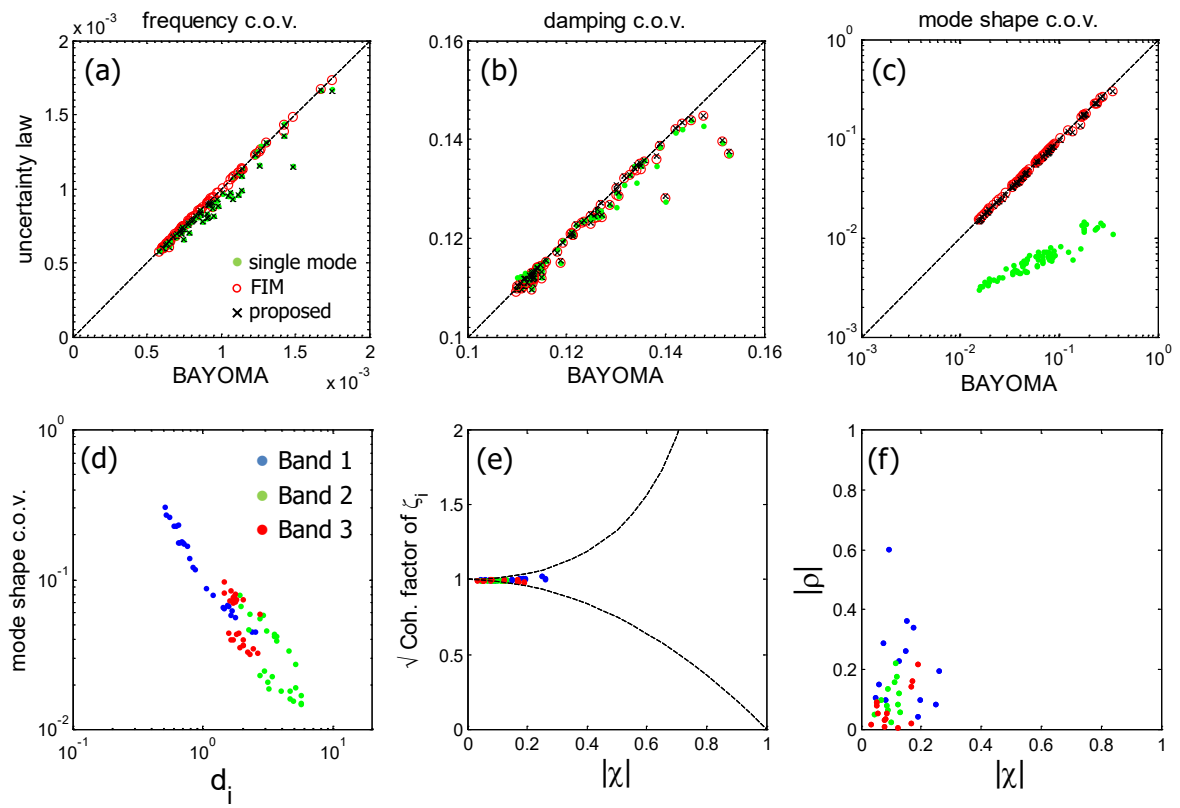**Figure 17 PSD and SV of a typical data set, Jiangyin Yangtze River Bridge**

Figure 18 Summary of results, Jiangyin Yangtze River Bridge. Same legend as Figure 10
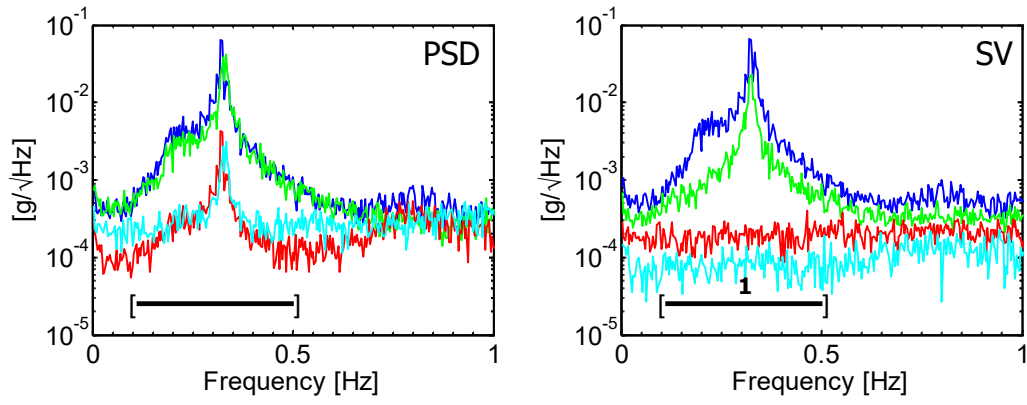
Figure 19 PSD and SV spectra of Rugeley Chimney
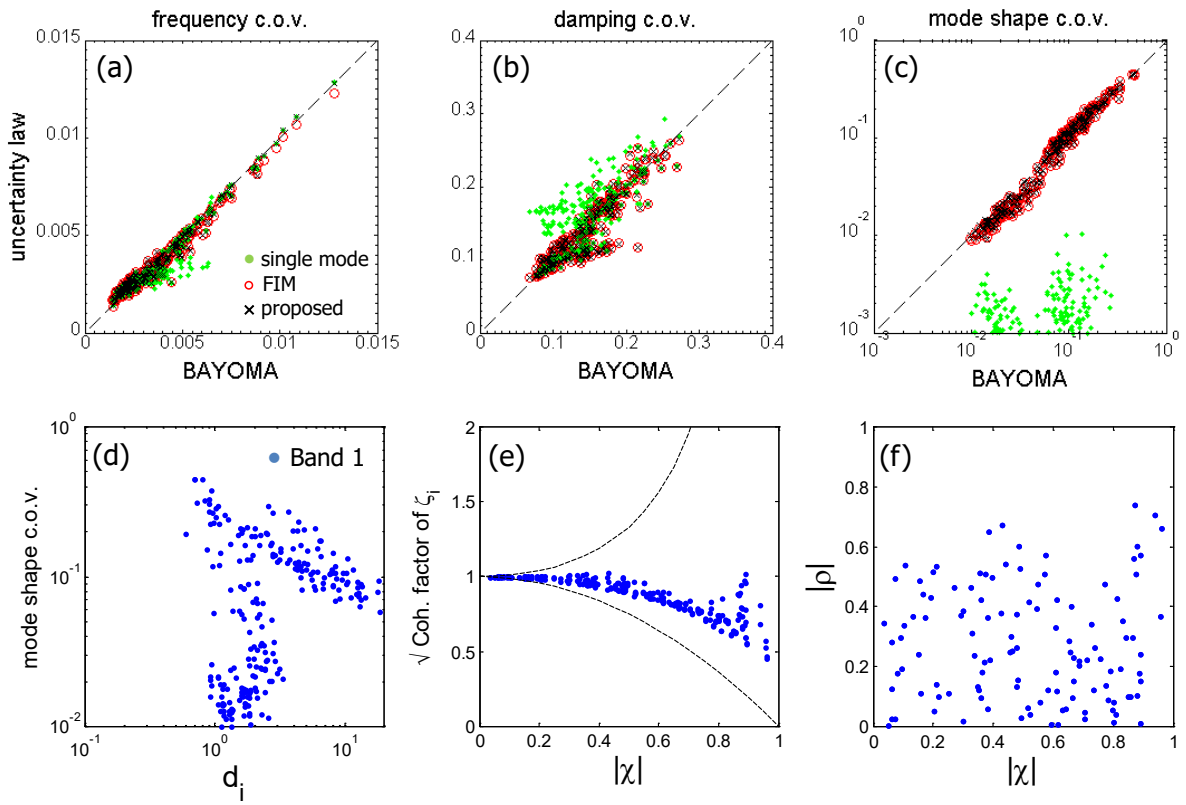

Figure 20 Summary of results, Rugeley Chimney. Same legend as Figure 10

6 Practical implication and recommendation

Well-separated modes are conventional subjects in modal ID. A logical way to think about the implications of uncertainty law of close modes developed in this work is to see what concepts or requirements need to be adjusted/introduced beyond those already in place for well-separated modes [39]. This is how the c.o.v.s of frequencies and damping ratios in (8) and (9) have been written. Close modes bring in the coherence factors Q_{f_i} and Q_{ζ_i} in (10) and (11). It is more useful to think of the coherence factors in terms of the bounds in (21); see also Figure 5. Further correction to capture the effect of bandwidth and s/n ratio is needed. This can be done using the empirical factors in Table 1, where the modal s/n ratio γ_i'' is equal to the old one for well-separated modes (γ_i') discounted by $(1-|\chi|^2)$ and $(1-\rho^2)$.

Close modes bring additional uncertain dimensions to mode shapes and this overturns our intuition about the governing uncertainty accumulated for well-separated modes. Mode shape uncertainty is no longer negligible. It can even render the problem unidentifiable. For well-separated modes it is always orthogonal to the identified mode shape direction (Type 1, see (2) and Figure 2) and is negligible for high s/n ratio. For close modes, Type 1 uncertainty remains to be negligible for high s/n ratio, but the additional non-vanishing uncertainty (Type 2, see (3)) smearing between mode shapes is of the same order of magnitude as or even larger than damping uncertainty. Based on (3), one can think of the mode shape c.o.v. (Type 2) as being equal to the damping c.o.v. amplified by the effects of disparities ($1/d_i$ and $\sqrt{S_{jj}/S_{ii}}$), MAC ($\sqrt{1-\rho}$) and coherence ($\sqrt{Q_{\varphi_i}}$). It is useful to think of Q_{φ_i} in terms of its upper bound, which coincides with those of frequency and damping in Figure 5. Accordingly, *doubling the c.o.v. will account for the effect of coherence in most cases*.

6.1 Planning for well-separated modes – what we already knew

Uncertainty law for well-separated modes was developed in [39] to allow one to manage quantitatively the ID uncertainty. In this case damping uncertainty is the governing factor and its c.o.v. is given by

$$\delta_\zeta = \frac{1}{\sqrt{2\pi\zeta N_c}} \times A_\gamma \times A_\kappa \qquad \text{(well-separated mode)} \qquad (29)$$

where ζ is the damping ratio (mode number omitted), N_c is the dimensionless duration as a multiple of natural periods, e.g., a duration of 100 sec for a 2Hz mode gives $N_c = 100 \times 2 = 200$;

A_γ and A_κ account for finite s/n ratio and bandwidth, respectively, and are calculated according to Table 1 with (omitting index i) γ'' replaced by $\gamma' = S/4S_e\zeta^2$. At the planning stage, data and hence the selected band is not available and so one may not be able to use (26) to assess κ. Instead, one may take $\kappa = \min(2\sqrt{\gamma'}, \kappa_{\max})$ to reflect that the usable bandwidth increases with s/n ratio γ' up to a limit $\kappa_{\max}$ set to control modelling error against, e.g., existence of unaccounted modes and assumption of locally flat modal force PSDs and noise PSDs. Equation (29) can be rewritten to give the required data duration (as a multiple of natural period):

$$N_c = \underbrace{\frac{1}{2\pi\zeta\delta_\zeta^2}}_{\substack{\text{'optimistic' min.}\\\text{req. duration}}} \times \underbrace{A_\gamma^2}_{\substack{\text{inflation due to}\\\text{finite s/n ratio}}} \times \underbrace{A_\kappa^2}_{\substack{\text{inflation due to}\\\text{finite bandwidth}}} \qquad \text{(well-separated mode)} \qquad (30)$$

6.2 Planning for close modes – what we did not know

Regardless of whether one has planned for close modes in ambient vibration tests, they can be encountered and present challenge to modal analysts. The knowledge generated in this work allows one to plan with a strong scientific basis. To cater for close modes, both damping and mode shape uncertainty need to be assessed. Equations (3) and (9) offer insights but their direct use requires too much detail and is not suitable for planning. Simple provisions are recommended here as an extension of those for well-separated modes. The damping c.o.v. can still be assessed using (29) but now with two modifications: 1) the value should be amplified by $\sqrt{Q_\zeta}$ in (11) (omitted mode index i) to account for coherence; and 2) the s/n ratio for evaluating A_γ and A_κ (via κ) in Table 1 should be $\gamma'' = \gamma'(1-\rho^2)(1-|\chi|^2)$ as in (26). The data duration (as a multiple of natural periods) required to achieve a c.o.v. of δ_ζ in the damping ratio is given by

$$N_c = \underbrace{\frac{1}{2\pi\zeta\delta_\zeta^2}}_{\substack{\text{'optimistic' min.}\\\text{req. duration}}} \times \underbrace{A_\gamma^2}_{\substack{\text{inflation due to}\\\text{finite s/n ratio}}} \times \underbrace{A_\kappa^2}_{\substack{\text{inflation due to}\\\text{finite bandwidth}}} \times \underbrace{Q_\zeta}_{\substack{\text{inflation due to}\\\text{modal force}\\\text{coherence}}} \qquad \text{(close modes)} \qquad (31)$$

Without specific information on $|\chi|$ and ρ, their choice is a compromise between practicality and conservatism. Figure 5 suggests that taking $Q_\zeta = 4$ will be conservative for $|\chi|$ up to 0.85, but this implies an inflation of four times in the data length compared to that without coherence effect. More practical solution may be achieved at the expense of slightly reduced conservatism, e.g., taking

$Q_\zeta = 2$ will allow for $|\chi|$ up to 0.7. Remarkably, taking $Q_\zeta = 1.25$ (only 25% inflation) is sufficient to allow for $|\chi|$ up 0.5, essentially because the bounding curve in Figure 5 is flat for small $|\chi|$. See Table 3 and Parts (e) and (f) of Figures 14, 16, 18 and 20 that report the statistics of $|\chi|$ in some field tests. On the other hand, the factor $(1-\rho^2)(1-|\chi|^2)$ in the s/n ratio γ'' may be conveniently taken as 1/2 or 1/4, which roughly correspond to $\rho = |\chi| = 0.5$ and $\rho = |\chi| = 0.7$, respectively. For the mode shape c.o.v., a simple rule is to take it *the same as* the damping c.o.v. and then assess whether it is acceptable with the help of Figure 3. This recommendation is based on (3), taking nominally $d_i = 1$, $S_{jj}/S_{ii} = 1$, somewhat conservatively $\rho = 0$ (so $1 - \rho^2 = 1$); and using the same upper bound for Q_{φ_i} and Q_{ζ_i}.

6.3 Example

Consider ambient vibration test planning where the data duration is often governed by the precision in the damping ratio of the mode with the lowest frequency. We shall first assume that the mode is well-separated and then see later the additional duration required to allow for the possibility of close modes. For the purpose of determining the data length, assume a damping ratio of 1% and a required c.o.v. of 30%, which represents a moderate precision. The first term in (30) gives the minimum required duration as $1/(2\pi \times 1\% \times 0.3^2)$, i.e., about 177 natural periods. This duration is optimistic because it assumes infinite bandwidth, infinite s/n ratio (noiseless channel). To account for these two effects, assume conservatively that a single triaxial servo-accelerometer is used, for which the noise PSD is $S_e = 1(\mu g)^2 / Hz$ and the modal force PSD is taken to be $S = 0.1(\mu g)^2 / Hz$ (typical in urban environment). The modal s/n ratio is then

$\gamma' = S/4S_e\zeta^2 = (0.1)/(4 \times 1 \times 0.01^2) = 250$. Taking $\kappa_{\max} = 10$, the usable bandwidth is

$\kappa = \min(2\sqrt{250}, 10) = 10$, which is controlled by modelling error risk because the s/n ratio is sufficiently high. Substituting $\gamma'' = 250$ and $\kappa = 10$, Table 1 gives $A_\gamma^2 \approx 1.083$ and $A_\kappa^2 \approx 1.381$, i.e., an inflation of 8% due to finite s/n ratio and 38% due to finite bandwidth. Consequently, the required data length to achieve a 30% c.o.v. in the damping ratio is

$N_c = (177)(1.083)(1.381) \approx 265$ natural periods. Using more or better sensors will not reduce this duration significantly because the s/n ratio is already high enough. The above procedure was proposed and related issues were discussed previously in the work of uncertainty law for well-separated modes [39], which may be consulted for further details and examples.

What provision should be made to account for the possibility of two close modes? In the first place, one should examine the adequacy of senor locations (or directions if uniaxial) for distinguishing the mode shapes of the two potentially close modes, so that the singular value spectrum of data will have two significant lines displaying dynamic amplification, reflecting a two-dimensional mode shape subspace. The following discussion assumes that the mode shapes are distinguishable; otherwise it is out of the scope of this work. Taking nominally $\rho = |\chi| = 0.5$ and hence

$(1-\rho^2)(1-|\chi|^2) = 0.56$, the s/n ratio is reduced by about half to $\gamma'' = (250)(0.56) = 140$. The

usable bandwidth is $\kappa = \min(2\sqrt{140}, 10) = 10$, i.e., still controlled by modelling error risk.

Substituting $\gamma'' = 140$ and $\kappa = 10$, Table 1 gives $A_\gamma^2 \approx 1.149$ and $A_\kappa^2 \approx 1.381$, i.e., an inflation of

15% (higher now since s/n ratio is reduced) and 38% (same as before since usable bandwidth remains the same). In addition to s/n and bandwidth effect, with close modes now we also need to account for modal force coherence effect. Taking $|\chi| = 0.5$ as before, $Q_\zeta = 1.25$ and so the data duration required for achieving a c.o.v. of 30% in damping ratio is

$N_c = (177)(1.149)(1.381)(1.25) \approx 351$ natural periods, about 32% longer than that for well-separated mode before. For assessment purpose the resulting mode shape c.o.v. is about 30% (taken to be the same as damping c.o.v.), which is marginally acceptable; see Figure 3. Better quality

in the mode shape with a c.o.v. of 10% will require $3^2 = 9$ times as much the data length, i.e.,

$351 \times 9 = 3159$ natural periods. Depending on the natural period, this duration may be too long to be practical or it may incur significant modelling error in data stationarity or time invariance in structural properties. Here we see that for close modes it is not practical to demand the same level of mode shape precision as for well-separated modes (c.o.v. often below 1%). There is also less room for conservatism, e.g., allowing for modal coherence up to 0.85 will require a further inflation in data length of $4/1.25 = 3.2$ times.

7   Conclusions

This work has made discoveries that allow one to understand the identification (ID) uncertainty of close modes in operational modal analysis (OMA) and manage it in ambient vibration tests. The asymptotic formulae for ID uncertainty reveal explicitly the effect of governing factors including the disparities in frequencies, damping ratios, modal force PSDs and their coherence, and mode shapes; see (8), (9) and (1). Mode shape uncertainty is most intriguing, extending into dimensions unique to close modes and prevailing even with noiseless data, therefore posing a new precision limit on OMA distinguished from the previously found limit for well-separated modes.

The mathematical theory for the uncertainty law of close modes is much more complicated than that for well-separated modes; see the companion paper [40]. The ID uncertainty admits a remarkably simple and insightful mathematical form when the resonance band containing information for identification is sufficiently wide. It has not been possible to derive mathematically rigorous formulae to capture the effects of finite bandwidth and signal-to-noise ratio. Instead, they are addressed by empirical correction factors; see Table 1. The investigation with field data reveals the source and mechanism of close mode uncertainty under various field situations. Modal disparities are of the order of 1 with low values around 0.5; see Table 3 for other statistics. In addition to damping, planning field tests considering close modes also involves managing mode shape uncertainty; see Section 6 for simple recommendations.

Some remarks are in order. Uncertainty laws are intended for understanding achievable precision limits and managing ID uncertainty in test planning where data is not available. When data is available the ID uncertainty should be calculated by a modal ID algorithm (e.g., BAYOMA) based on the particular data set. Uncertainty laws are developed based on the same set of modelling assumptions in the modal ID algorithm (except for the asymptotic conditions), and so they do not reflect modelling error. The latter should be judged or controlled by other means, e.g., avoiding excessively long time windows to justify stationarity. Although acceleration data is often referred, this work is also applicable to other data types (e.g., velocity, displacement) provided that the s/n ratio is defined in a consistent manner; see Section 6.6 in the companion paper.

8 Acknowledgements

9 Appendix. Supplementary data

The research materials supporting this publication can be accessed by contacting ivanau@ntu.edu.sg.

10 Appendix. Proof of (17) and (18)

In (17), the inequality $q_1^2 \leq q_2^2$ follows directly from $q_1 = q_2 \sin(2\phi - \psi)$. The inequality $q_2^2 \leq 1$ can be reasoned as follow. First note that

$$q_2^2 = g_1^2 + g_2^2 = \frac{4}{|e_1 e_2| + (c_1 + 2)(c_2 + 2)} \leq \frac{4}{(c_1 + 2)(c_2 + 2)} \leq 1 \tag{32}$$

since

$$(c_1 + 2)(c_2 + 2) = (\frac{f_2 \zeta_2}{f_1 \zeta_1} + 1)(\frac{f_1 \zeta_1}{f_2 \zeta_2} + 1)$$
$$= 2 + \frac{f_2 \zeta_2}{f_1 \zeta_1} + \frac{f_1 \zeta_1}{f_2 \zeta_2} \geq 4 \qquad (x + x^{-1} \geq 2 \text{ for } x \geq 0) \tag{33}$$

It then follows that $g_i^2 \leq g_1^2 + g_2^2 = q_2^2 \leq 1$. In (18), the leftmost inequality is trivial. The second inequality follows from $1 \leq (1 - q_2^2 |\chi|^4)/(1 - q_2^2 |\chi|^2)$ because $|\chi|^4 \leq |\chi|^2$. The third inequality follows from $1 \leq (1 - q_2^2 |\chi|^4)/(1 - q_1^2 |\chi|^4)$ because $q_1^2 \leq q_2^2$.

The inequalities in (17) and (18) are attainable and therefore they are the tightest possible ones. For (17), $q_1 = 0$ when $2\phi - \psi = 0$; $q_1 = q_2$ when $2\phi - \psi = \pm \pi/2$; $q_2 = 1$ when $d_i = 0$. For (18), $1/(1 - q_1^2 |\chi|^4) = 1$ when $q_1 = 0$ or $|\chi| = 0$; $Q_{\phi_i} = 1/(1 - q_1^2 |\chi|^4)$ when $|\chi| = 1$; $Q_{\phi_i} = 1/(1 - q_2^2 |\chi|^4)$ when $q_1 = q_2$; $1/(1 - q_2^2 |\chi|^2) = 1/(1 - |\chi|^2)$ when $q_2 = 1$.

11 Appendix. Proof of (19)

From (12), underestimating the second term gives the lower bound in (19):

$$R_{f_i} \geq (1 - q_2^2 |\chi|^2)^2 \cos^2(\phi - s_i \phi_i) + (1 - |\chi|^2)^2 q_2^2 \sin^2(\phi + s_i \phi_i - \psi)$$
$$- 2|q_1| |\chi|^2 (1 - q_2^2 |\chi|^2)(1 - |\chi|^2) q_2 |\cos(\phi - s_i \phi_i) \sin(\phi + s_i \phi_i - \psi)|$$
$$= \left[(1 - q_2^2 |\chi|^2) \cos(\phi - s_i \phi_i) - (1 - |\chi|^2) q_2 \sin(\phi + s_i \phi_i - \psi) \right]^2$$
$$+ 2(1 - |q_1| |\chi|^2)(1 - q_2^2 |\chi|^2)(1 - |\chi|^2) q_2 |\cos(\phi - s_i \phi_i) \sin(\phi + s_i \phi_i - \psi)| \geq 0 \tag{34}$$

On the other hand, over-estimating the second term in (12) gives

$$R_{f_i} \leq (1 - q_2^2 \mid \chi \mid^2)^2 \cos^2(\phi - s_i \phi_i) + (1 - \mid \chi \mid^2)^2 q_2^2 \sin^2(\phi + s_i \phi_i - \psi)$$

$$+ 2 \mid q_1 \parallel \chi \mid^2 (1 - q_2^2 \mid \chi \mid^2)(1 - \mid \chi \mid^2) q_2 \mid \cos(\phi - s_i \phi_i) \sin(\phi + s_i \phi_i - \psi) \mid \qquad (35)$$

Overestimating $\mid q_1 \mid$ by q_2, the sines and cosines by 1, and simplifying gives the upper bound in (19). The lower and upper bounds of R_{f_i} can be attained by setting $f_1 = f_2$ and additionally $\phi = 0$ (lower bound) or $\phi = \pi / 2$ (upper bound). In particular, when $f_1 = f_2$, $e_i = 0$. Then $g_2 = 0$ and so $\psi = \pi / 2$. Also, $\tan \phi_i = c_i / e_i = \infty$ gives $\phi_1 = \pi / 2$ and $\phi_2 = -\pi / 2$ (one possibility). Substituting ϕ_1, ϕ_2 and ψ into (12) gives

$$R_{f_i} = (\sin^2 \phi) \times$$

$$[(1 - q_2^2 \mid \chi \mid^2)^2 + (1 - \mid \chi \mid^2)^2 q_2^2 - 2 \mid \chi \mid^2 q_2^2 (1 - q_2^2 \mid \chi \mid^2)(1 - \mid \chi \mid^2)(1 - 2 \sin^2 \phi)] \qquad (36)$$

Further substituting $\phi = 0$ and $\phi = \pi / 2$ gives the bounding values in (19). The reasoning for R_{ζ_i} is the same except that (in addition to $f_1 = f_2$) $\phi = \pi / 2$ gives the lower bound and $\phi = 0$ gives the upper bound.

12 References

[1] M.I. Friswell, J.E. Mottershead, Finite element model updating in structural dynamics, Kluwer Academic Publishers, Dordrecht, 1995.

[2] J.M.W. Brownjohn, Structural health monitoring of civil infrastructure, Philosophical Transactions of the Royal Society of London A: Mathematical, Physical and Engineering Sciences 365(1851) (2007) 589-622.

[3] C.R. Farrar, K. Worden, Structural health monitoring: a machine learning perspective, Wiley, London, 2012.

[4] Y.L. Xu, Y. Xia, Structural Health Monitoring of Long-span Suspension Bridges, Spon Press (Taylor& Francis), UK, 2012.

[5] F.N. Catbas, T. Kijewski-Correa, A.E. Aktan (eds), Structural Identification of Constructed Systems: Approaches, Methods, and Technologies for Effective Practice of St-Id, American Society of Civil Engineers, 2011.

[6] D.J. Ewins, Modal testing: Theory and practice, Research Studies Press, PA, USA, 2000.

[7] N. Maia, J. Silva, Theoretical and experimental modal analysis, Research Studies Press Ltd, Baldock, 1997.

[8] Wenzel H, Pichler D (2005) Ambient Vibration Monitoring. John Wiley & Sons, UK

[9] R. Brincker, C. Ventura, Introduction to operational modal analysis, Wiley, London, 2015.

[10] S.K. Au, Operational Modal Analysis: Modelling, Inference, Uncertainty Laws. Springer, Singapore, 2017.

[11] C.Y. Shih, Y.G. Tsuei, R.J. Allemang, D.L. Brown, Complex mode indication function and its application to spatial domain parameter estimation, Mechanical Systems and Signal Processing, 2(4) (1988) 367-377.

[12] S.K. Au, F.L. Zhang, P. To, Field observations on modal properties of two tall buildings under strong wind, Journal of Wind Engineering and Industrial Aerodynamics, 101 (2012) 12-23.

[13] F.L. Zhang, C.E. Ventura, H.B. Xiong, W.S. Lu, Y.X. Pan, J.X. Cao, Evaluation of the dynamic characteristics of a super tall building using data from ambient vibration and shake table tests by a Bayesian approach, Structural Control and Health Monitoring, 25(4) (2017) e2121.

[14] M.J. Glanville, K.C.S. Kwok, Dynamic characteristics and wind induced response of a steel frame tower, Journal of Wind Engineering and Industrial Aerodynamics, 54–55 (1995) 133-149.

[15] A.P. Jeary, Damping measurements from the dynamic behaviour of several large multi-flue chimneys, Proceedings of the Institution of Civil Engineers, 57(2) (1974) 321-329.

[16] J.M.W. Brownjohn, E.P. Carden, C.R. Goddard, G. Oudin, Real-time performance monitoring of tuned mass damper system for a 183 m reinforced concrete chimney, Journal of Wind Engineering and Industrial Aerodynamics, 98(3) (2010) 169-179.

[17] A. DeVivo, C. Brutti, J.L. Leofanti, Modal shape identification of large structure exposed to wind excitation by operational modal analysis technique, Mechanical Systems and Signal Processing, 32(1-2) (2013) 195-206.

[18] J.M.W Brownjohn, A. Raby, J. Bassitt, A. Antonini, E. Hudson, P. Dobson, Experimental modal analysis of British rock lighthouses, Marine Structures, 62 (2018) 1-22.

[19] J.M.W. Brownjohn, F. Magalhaes, E. Caetano, A. Cunha, Ambient vibration re-testing and operational modal analysis of the Humber Bridge, Engineering Structures, 32(8) (2010) 2003-2018.

[20] A. Der Kiureghian, Structural Response to Stationary Excitation, Journal of the Engineering Mechanics Division 106 (1980) 1195–1213.

[21] A. Der Kiureghian, A response spectrum method for random vibration analysis of mdf systems, Earthquake Engineering & Structural Dynamics **9**(5) (1981) 419–435.

[22] E.L. Wilson EL, A. Der Kiureghian, E.P. Bayo, A replacement for the srss method in seismic analysis, Earthquake Engineering & Structural Dynamics, **9**(2) (1981) 187–192.

[23] W. D'Ambrogio, A. Fregolent, High-order MAC for the correlation of close and multiple modes, Mechanical Systems and Signal Processing,17(3) (2003) 599–610.

[24] R. Brincker, M. Lopez-Aenlle, Mode shape sensitivity of two closely spaced eigenvalues, Journal of Sound and Vibration, 334 (2015) 377–387.

[25] R. Brincker, Implication of closely spaced modes in OMA, 6th International Operational Modal Analysis Conference, Gijón, Spain, 2015.

[26] A. Bajrić, R. Brincker, Thöns S. Evaluation of damping estimates in the presence of closely spaced modes using operational modal analysis techniques, *6th International Operational Modal Analysis Conference*, Gijon, Spain, 2015.

[27] L. Zhang, T. Wang, Y. Tamura, A frequency–spatial domain decomposition (FSDD) method for operational modal analysis, Mechanical Systems and Signal Processing, 24(5) (2010) 1227–1239.

[28] S.K. Au, Fast Bayesian ambient modal identification in the frequency domain, Part I: posterior most probable value, Mechanical Systems and Signal Processing 26(1) (2012) 60-75.

[29] S.K. Au, Fast Bayesian FFT method for ambient modal identification with separated modes, Journal of Engineering Mechanics, ASCE, 137(3) (2011) 214-226.

[30] B.B. Li, S.K. Au (2019), An expectation-maximization algorithm for Bayesian operational modal analysis with multiple (possibly close) modes". Mechanical Systems and Signal Processing, 132: 490-511.

[31] J.M. Caicedo, Practical guidelines for the natural excitation technique (NExT) and the eigensystem realization algorithm (ERA) for modal identification using ambient vibration. Experimental Techniques, 35(4) (2011) 52–58.

[32] S.A.A. Hosseini Kordkheili, S.H.H. Momeni Massouleh, S. Hajirezayi, H. Bahai, Experimental identification of closely spaced modes using NExT-ERA, Journal of Sound and Vibration, 412 (2018) 116–129.

[33] B. Peeters, C.E. Ventura, Comparative study of modal analysis techniques for bridge dynamic characteristics, Mechanical Systems and Signal Processing, 17(5) (2003) 965–988.

[34] B. Peeters, H. Van der Auweraer, F. Vanhollebeke, P. Guillaume, Operational Modal Analysis for Estimating the Dynamic Properties of a Stadium Structure during a Football Game, Shock and Vibration, 14(4) (2007) 283–303.

[35] F. Magalhaes, E. Caetano, A. Cunha, Challenges in the Application of Stochastic Modal Identification Methods to a Cable-Stayed Bridge, Journal of Bridge Engineering, 12(6) (2007) 746–754.

[36] A. Srikantha Phani, J. Woodhouse, Viscous damping identification in linear vibration, Journal

of Sound and Vibration, 303(3–5) (2007) 475–500.

[37]   Y.C. Zhu, S.K. Au, S. Jones, Uncertainty of Closely-Spaced Modes in Bayesian Modal
       Identification, Proc. Engineering Mechanics Institute Conference 2015 Conference, 16-19 Jun
       2015, San Francisco, California, USA, 2015.

[38]   P. Sun, Y. Ding, J. Zhang, A. Li, Y. Deng, Modal identification of closely spaced modes based on
       Morlet wavelet transform, 42(2) (2012) 339-345.

[39]S.K. Au, J.M.W. Brownjohn, J.E. Mottershead, Quantifying and managing uncertainty in
    operational modal analysis, Mechanical Systems and Signal Processing, 102 (2017) 139-157.

[40]S.K. Au, B. Li, J.M.W. Brownjohn, Achievable precision of close modes in operational modal
    analysis: wide band theory, Mechanical Systems and Signal Processing, companion paper, under
    review.

[41]S.K. Au, J.M.W. Brownjohn, Asymptotic identification uncertainty of close modes in Bayesian
    operational modal analysis, Mechanical Systems and Signal Processing. DOI:
    10.1016/j.ymssp.2019.106273

[42]E.T. Jaynes, Probability Theory: The Logic of Science. Cambridge University Press, UK, 2003.

[43]J.L. Beck JL, Bayesian system identification based on probability logic, Structural Control and
    Health Monitoring 17(7) (2010) 825-847.

[44]J.M.W. Brownjohn, S.K. Au, Y.C. Zhu, S. Zhen, B.B. Li, J. Bassit, E. Hudson, H.B. Sun, Ambient
    vibration test of Jiangyin Yangtze River Bridge, Mechanical Systems and Signal Processing, 110
    (2018) 210-230.

[45]   S.K. Au, B.B. Li, Posterior uncertainty, asymptotic law and Cramer Rao Bound, Structural
       Control and Health Monitoring, 25(3) (2017) DOI: 10.1002/stc.2113